

Non-Fickian Transport in Transparent Replicas of Rough-Walled Rock Fractures

Ali Nowamooz · Giovanni Radilla · Mostafa Fourar · Brian Berkowitz

Received: 14 August 2012 / Accepted: 17 April 2013 / Published online: 7 May 2013
© Springer Science+Business Media Dordrecht 2013

Abstract We present an experimental investigation and modeling analysis of tracer transport in two transparent fracture replicas. The original fractures used in this work are a Vosges sandstone sample with nominal dimensions approximately 26 cm long and 15 cm wide, and a granite sample with nominal dimensions approximately 33 cm long and 15.5 cm wide. The aperture map and physical characteristics of the fractures reveal that the aperture map of the granite fracture has a higher spatial variability than the Vosges sandstone one. A conservative methylene blue aqueous solution was injected uniformly along the fracture inlets, and exited through free outlet boundaries. A series of images was recorded at known time intervals during each experiment. Breakthrough curves were subsequently determined at the fracture outlets and at different distances, using an image processing based on the attenuation law of Beer–Lambert. These curves were then interpreted using a stratified medium model that incorporates a permeability distribution to account for the fracture heterogeneity, and a continuous time random walk (CTRW) model, as well as the classical advection–dispersion equation (ADE). The stratified model provides generally satisfactory matches to the data, while the CTRW model captures the full evolution of the long tailing displayed by the breakthrough curves. The transport behavior is found to be non-Fickian, so that the ADE is not

A. Nowamooz (✉) · G. Radilla · M. Fourar
LEMTA, Nancy-University, CNRS, 2 avenue de la Forêt de Haye, BP 160,
54504 VANDOEUVRE CEDEX, France
e-mail: Ali.Nowamooz@ensam.fr

M. Fourar
e-mail: Mostafa.Fourar@mines.inpl-nancy.fr

A. Nowamooz · G. Radilla
Arts et Métiers ParisTech, rue St Dominique, BP 508, 51006
Châlons-en-Champagne, France
e-mail: Giovanni.Radilla@ensam.fr

B. Berkowitz
Department of Environmental Sciences and Energy Research,
Weizmann Institute of Science, 76100 Rehovot, Israel
e-mail: Brian.Berkowitz@weizmann.ac.il

applicable. In both stratified and CTRW models, parameter values related to the aperture field spatial variability indicate that the granite fracture is more heterogeneous than the Vosges sandstone fracture.

Keywords Rough fractures · Heterogeneous media · Anomalous transport · Breakthrough curves · Equivalent-stratified porous medium · Continuous time random walk

List of Symbols

a	Power law constant, Eq. (16)
α	Dispersivity (m)
b	Power law exponent, Eq. (16)
β	Exponent, Eq. (8)
C	Concentration (g/l)
C^*	Dimensionless concentration
C_0	Injected concentration (g/l)
D	Dispersion coefficient (m ² /s)
D_m	Molecular diffusion coefficient (m ² /s)
D_ψ	Transport dispersion coefficient (m ² /s)
ε	Solute absorptivity (m ² /g)
$G(k)$	Probability distribution function of the permeability
γ	(Semi)variogram (mm ²)
H	Heterogeneity factor
h	Thickness or local aperture (mm)
$\langle h \rangle$	Mean aperture (mm)
I	Intensity
I_0	Intensity at $C = 0$
k	Permeability ($k = h^2/12$) (m ²)
$\langle k \rangle$	Mean permeability (m ²)
L_x	Fractures length (m)
L_y	Fractures wide (m)
M	Memory function
μ	Dynamic viscosity (mPa s)
N	Number of measured values, Eq. (15)
N_r	Number of pairs, Eq. (11)
P	Pressure (Pa)
$p(s)$	Probability distribution of transition displacements
Pe	Peclet number
Q	Flow rate (ml/h)
$RMSE$	Root-mean-square error
ρ	Density (kg/m ³)
σ	Standard deviation
t	Time (s)
t^*	Dimensionless time
t_1	Median transition time in ψ (s)
t_2	Cutoff time in ψ (s)
U	Average fluid velocity (m/s)
u_ψ	Transport velocity (m/s)

V_p	Pore volume (ml)
w	Laplace variable
x	Location in space (m)
x^*	Dimensionless distance
y	Location in space (m)
$\psi(t)$	Probability rate for a transition time t

1 Introduction

Quantifying solute transport in fractured media has been an important research topic in hydrology over the last three decades. This has been motivated at least in part by consideration of storage and disposal of radioactive waste and CO₂ in fractured geological formations, and by efforts to remediate contaminated, fractured groundwater reservoirs. A key foundation of such studies has thus been analysis of fluid flow and solute transport in individual rock fractures. While early studies considered simplified parallel plate or sinusoidal fracture wall geometries, more realistic investigations examine tracer transport in natural, rough-walled fractures.

Flow and transport in fractures are influenced significantly by the natural heterogeneity of fractures, as a result of fracture wall roughness (Dronfield and Silliman 1993; Ippolito et al. 1993; Yeo 2001) and the resulting aperture distribution (Moreno et al. 1988; Tsang et al. 1991; Nordqvist et al. 1996; Detwiler et al. 2000). In general, the high degree of variability in natural heterogeneities prevents acquisition of detailed knowledge of the pore space in which tracer migrates.

The advection–dispersion equation (ADE) has been applied, traditionally, to model tracer transport in fractures. However, several laboratory scale tracer tests in single fractures reported significant deviations between measured breakthrough curves (BTCs) and curves obtained using the ADE (e.g., Neretnieks et al. 1982; Becker and Shapiro 2000; Jiménez-Hornero et al. 2005; Bauguet and Fourar 2008). More specifically, in these analyses, the ADE did not capture the non-Fickian (or anomalous) behavior exemplified in the early breakthrough times (i.e., later than Fickian) and long-time tailing.

Modeling non-Fickian tracer transport in fractured and porous media has received considerable attention in recent years. Fourar (2006) proposed the equivalent-stratified medium approach to describe anomalous transport and applied it to solute transport in heterogeneous porous media (Fourar 2006; Fourar and Radilla 2009) and a single rough-walled rock fracture (Bauguet and Fourar 2008). The basic idea of this approach is to represent a heterogeneous medium by using an equivalent-stratified medium, for which the tracer transport can be modeled in a consistent manner. This approach also assumes statistical homogeneity of the medium (i.e., the permeability of the medium is a probability distribution function) but introduces a “heterogeneity factor” as a parameter that evolves along the paths experienced by the tracer. Recently, Radilla et al. (2012) applied this approach to accurately model field-scale tracer tests performed in the Soultz-sous-Forêts Enhanced Geothermal System.

A powerful framework to describe non-Fickian transport in fractured and heterogeneous porous media is offered by the continuous time random walk (CTRW) approach (Berkowitz et al. 2006). CTRW is based on the conceptual picture of tracer particles undergoing a series of transitions, characterized by a distribution of transition times. The physics and/or geochemical mechanisms involved in the transport process, as well as the structure of the heterogeneous

porous or fractured medium or nature of the flow regime, determine the relevant transition time distribution and control the interpretation of its parameters. In the CTRW framework, a solute particle undergoes a series of transitions of length s and time t . Together with a master equation conserving solute mass, the random walk is developed into a transport equation in partial differential equation form. The CTRW has been successfully applied for describing the non-Fickian transport in heterogeneous porous media (Levy and Berkowitz 2003; Xiong et al. 2006; Berkowitz and Scher 2008; Gao et al. 2009), single fractures (Berkowitz et al. 2001; Jiménez-Hornero et al. 2005; Bauguet and Fourar 2008), and field tracer migration (Berkowitz and Scher 1997; Kosakowski et al. 2001).

Laboratory scale single fractures have been applied successfully to examine aspects of non-Fickian transport over the last two decades. For example, Neretnieks et al. (1982) examined nonsorbing tracer transport in a single natural fissure in a granitic sample, and attributed the BTC behavior to preferential channeling related to the aperture variations in the fracture plane. Moreno et al. (1985) also examined nonsorbing tracer dispersion in a single fracture in granite and concluded that BTCs can be modeled by both hydrodynamic and channeling diffusive mechanisms. Jiménez-Hornero et al. (2005) analysed the experimental data of Moreno et al. (1985) using CTRW, interpreting the moderately dispersive transport behavior to the presence of small and intermediate scale heterogeneities. Bauguet and Fourar (2008) focused on non-Fickian dispersion in a transparent replica of a real Vosges sandstone fracture, studying the ability of the ADE, equivalent-stratified medium, and CTRW approaches to describe the non-Fickian behavior as well as possible correlations between model fitting parameters and the spatial variability of the fracture aperture field. However, predictive modeling of fracture transport remains limited and thus further laboratory-scale studies are needed both to establish the transport characteristics of single fractures and to provide experimental data sets for model testing.

Models of tracer transport are most frequently applied to measured breakthrough curves at a porous medium column or fracture outlet, characterizing dispersion properties from overall medium properties. Several studies have examined breakthrough curves measured at several distances from the porous media inlet (e.g., Berkowitz et al. 2000; Gao et al. 2009; Fourar and Radilla 2009). To our knowledge, though, less attention has been paid to measurement and analysis of tracer transport in single fractures with high spatial variability in the aperture fields, considering breakthrough curves at multiple distances (Bauguet and Fourar 2008). There are inherent difficulties in measuring the void geometry of individual rock fractures at sufficient resolution. However, transparent resin or molten-glass replicas of rough-walled rock fractures have been used successfully to study aperture fields (Detwiler et al. 1999; Wan et al. 2000; Isakov et al. 2001), identify dispersive flow regimes (Brown et al. 1998; Detwiler et al. 2000) and examine different approaches to describe the non-Fickian tracer transport (Bauguet and Fourar 2008).

The goal of this work is to study conservative tracer transport in two transparent replicas of rough-walled rock fractures without the presence of matrix diffusion, focusing on evolution of breakthrough curves as a function of distance. The transport behavior is strongly affected by the spatial variability of the aperture field. We first review solutions for one-dimensional tracer transport within the equivalent-stratified medium and CTRW approaches. We then describe the experimental set-up and procedures; we discuss how image processing based on the Beer–Lambert attenuation law can be used to determine average temporal breakthrough curves along the flow direction. We then investigate the ability of the two modeling approaches to match the breakthrough curves, and examine variation of model parameters with distance.

2 Theory

2.1 The equivalent-stratified medium approach

Transport in stratified media has been considered frequently in the groundwater literature as a suitable alternative for modeling transport in geological media (Güven et al. 1984; Communar 1998; Zavala-Sanchez et al. 2009; Bolster et al. 2010).

The main idea of this approach is to replace a heterogeneous fractured or porous medium by an equivalent-stratified medium. This approach supposes that: (i) the displacement of tracer in each layer is piston-like, (ii) mass transfer across the layers is negligible (flow is parallel to the layers), so that the layer positions do not modify the tracer spreading front and the spatial distribution of layers can be changed to facilitate the concentration calculations, (iii) the porosity of the medium is uniform, (iv) pore-scale dispersion and molecular diffusion are negligible, and (v) the permeability of the layers is randomly distributed (constant for each layer but can change from one layer to another).

For the case of a continuous injection at constant flow rate Q and concentration C_0 at $x = 0$, the concentration at position x and time t is given by [see Fourar and Radilla (2009) for more details]:

$$\frac{C(x, t)}{C_0} = \int_{k^* = \frac{x(k)}{Ut}}^{k_{\max}} G(k) dk \tag{1}$$

where U is the average fluid velocity, $G(k)$ is the probability distribution function (pdf) of the permeability k , k_{\max} is the maximum permeability value, k^* is the permeability of the layer where tracer front reaches position x at time t and $\langle k \rangle$ is the mean permeability.

To calculate the concentration, an adequate pdf of the permeability must be chosen. Numerous studies at various problem scales and in different geological settings have shown that fracture apertures, and therefore local permeabilities, follow normal (Hakami and Larsson 1996; Oron and Berkowitz 1998; Sharifzadeh et al. 2004) or lognormal (Iwano and Einstein 1993; Johns et al. 1993; Pyrak-Nolte et al. 1997) distributions:

$$G(k) = \frac{1}{\sigma_k \sqrt{2\pi}} \exp\left(-\frac{(k - \langle k \rangle)^2}{2\sigma_k^2}\right) \text{ (normal distribution)} \tag{2}$$

$$G(k) = \frac{1}{\sigma_{\ln k} \sqrt{2\pi} k} \exp\left(-\frac{(\ln k - \langle \ln k \rangle)^2}{2\sigma_{\ln k}^2}\right) \text{ (lognormal distribution)} \tag{3}$$

where σ_k^2 and $\sigma_{\ln k}^2$ are the variance of k and $\ln k$, respectively.

Substituting the expressions of $G(k)$ in Eq. 1 and performing the integrations yields the following equations for the stratified approach using normal and lognormal permeability distributions, respectively (Fourar 2006; Bauguet and Fourar 2008; Fourar and Radilla 2009):

$$\frac{C(x, t)}{C_0} = \frac{1}{2} \operatorname{erfc}\left(\frac{\frac{x}{Ut} - 1}{H\sqrt{2}}\right) \tag{4}$$

$$\frac{C(x, t)}{C_0} = \frac{1}{2} \operatorname{erfc}\left(\frac{\ln\left(\frac{x}{Ut}\sqrt{1+H^2}\right)}{\sqrt{2}\ln(1+H^2)}\right) \tag{5}$$

where, in both equations, H is the ‘‘heterogeneity factor’’ defined by the ratio of the standard deviation and the average permeability:

$$H = \frac{\sigma_k}{\langle k \rangle} \quad (6)$$

As explained above, the purpose of the equivalent-stratified medium is to provide a permeability distribution of a stratified medium which allows the best match between the modeled and the measured tracer concentration curves. Equations (4) and (5) are analytical expressions for the BTCs, controlled by a single parameter H , and leading to a robust and quickly converging parameter estimation approach. Also, these analytical solutions allow a straightforward quantitative comparison of the level of spatial variability in terms of aperture field maps. Discussion of methods for numerical determination of a permeability distribution that provides an exact match to the BTCs is beyond the scope of this paper.

It is important to note that the equivalent stratified medium and the real heterogeneous medium share the same total flow rate, the same global pressure drop (i.e., between the inlet and the outlet), and the same mean permeability. As a result, the flow velocity in a given layer of the equivalent medium is constant from the inlet to the outlet and the pressure drop is linear. This approach can lead to a reasonable description of transport in highly layered medium. To use it for heterogeneous fractures, we assume that the fractures can be represented by an equivalent-stratified medium with a given value of H . Because the breakthrough curve at the outlet contains information about all the flow paths, the heterogeneity factor can be used to roughly measure the level of heterogeneity (or level of spatial variability of the aperture field) of a fracture.

2.2 The continuous time random walk (CTRW) approach

The CTRW framework has been shown to be effective for describing non-Fickian transport behavior of a tracer flowing through porous and fractured media (Berkowitz and Scher 1997; Margolin and Berkowitz 2000; Dentz et al. 2003; Berkowitz et al. 2006). In the CTRW framework, transport is modeled as a sequence of particle transitions with displacement \mathbf{s} and time t , with a probability density $\psi(\mathbf{s}, t)$ (see Berkowitz et al. 2006 for a detailed review).

Considering the decoupled form $\psi(\mathbf{s}, t) = p(\mathbf{s})\psi(t)$, where $p(\mathbf{s})$ is the probability distribution of transition displacements and $\psi(t)$ is the probability rate for a transition time t between sites, the CTRW 1-D transport equation in Laplace space can be written as:

$$w\tilde{C}(x, w) - C_0 = -\tilde{M}(w) \left[u_\psi \frac{\partial \tilde{C}(x, w)}{\partial x} - D_\psi \frac{\partial^2 \tilde{C}(x, w)}{\partial x^2} \right] \quad (7)$$

where w is the Laplace variable, $\tilde{M}(w) = t_1 w \frac{\tilde{\psi}(w)}{1 - \tilde{\psi}(w)}$ is a memory function that captures the anomalous transport induced by unresolved heterogeneities, t_1 is a characteristic time for transition between sites, u_ψ and D_ψ are the average transport velocity and generalized dispersion coefficient, respectively, and the Laplace transform of a function $f(t)$ is represented by $\tilde{f}(w)$. As discussed by Berkowitz et al. (2006), it is important to note that the transport velocity can be different from the mean fluid velocity. Also, the generalized dispersion coefficient is distinct from that in the ADE. Note that, in contrast, Fickian-based models assume that the center of mass of the tracer plume moves with the average fluid velocity, and that the dispersion behaves macroscopically as a Fickian process, with the dispersivity being assumed constant in space and time. This means that the heterogeneities (i.e., spatial variability of the fracture aperture field) are neglected at the scale of interest and the medium is considered homogeneous (i.e., two parallel plates in context of this paper).

The probability density function $\psi(t)$ is a key aspect of the CTRW approach, which characterizes the nature of the transport. We employ a truncated power law (TPL) that also allows a transition from non-Fickian behavior to Fickian behavior at large times:

$$\psi(t) = t_1^{-1} \left\{ \left(\frac{t_1}{t_2} \right)^\beta \exp\left(\frac{t_1}{t_2}\right) \Gamma\left(-\beta, \frac{t_1}{t_2}\right) \right\}^{-1} \exp(-t/t_2) \left(1 + \frac{t}{t_1}\right)^{-1-\beta} \quad (8)$$

where β is a measure of the dispersive transport, t_2 is the cut-off time to Fickian behavior and $\Gamma(a, x)$ is the incomplete gamma function. With the TPL transition time distribution function, the very nature of solute transport can be characterized by the value of β which falls into three possible ranges. The case of $0 < \beta < 1$ describes the most anomalous transport where both the mean and standard deviation of the tracer plume scale as power laws with time. For $1 < \beta < 2$, solute transport is anomalous where the mean plume velocity is constant in time and the standard deviation retains a power law scaling. When $\beta > 2$, solute transport is Fickian and the CTRW equation simplifies to the ADE. The TPL scales as $\psi(t) \approx (t/t_1)^{-1-\beta}$ for $t_1 < t < t_2$ (the transport behavior is anomalous in this time regime) and decreases exponentially $\psi(t) \approx e^{-t/t_2}$ for $t \gg t_2$ (Fickian behavior may be reached at a time scale longer than t_2).

3 Experimental Procedure

The schematic of the experimental setup is shown in Fig. 1. The apparatus was designed to measure the concentration of immiscible fluid as it flows through a transparent replica of a natural fracture. The centerpiece of the apparatus is a transparent epoxy resin cast of both sides of the natural rough-walled rock fractures. The original fractures used in this work are a Vosges sandstone sample with nominal dimensions approximately 26 cm long and 15 cm wide and a granite sample with nominal dimensions approximately 33 cm long and 15.5 cm wide.

To create the transparent epoxy resin casts of the fractures surfaces, the same method described by Isakov et al. (2001) was used. In this method, each fracture half of the block

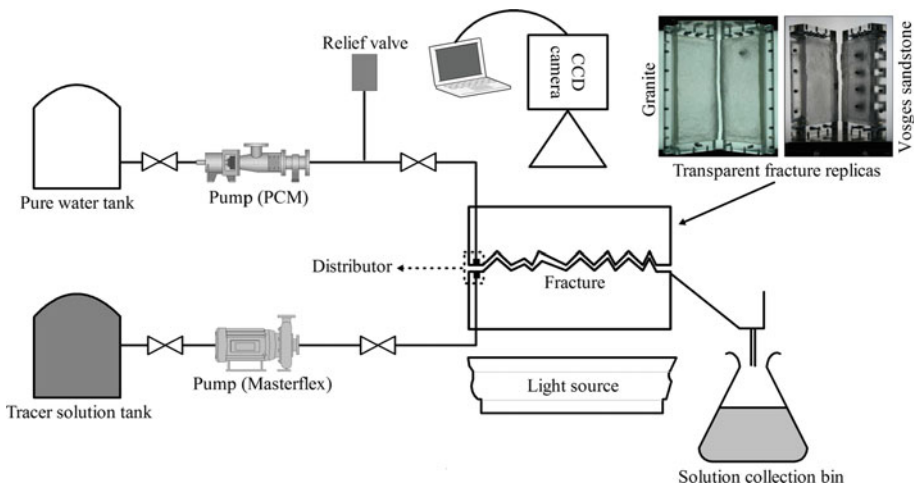


Fig. 1 Schematic of the Experimental Setup

was cleaned with compressed air and placed on a smooth working plate. Thin polycarbonate walls were added to the side of the sample and a thin layer of Silastic (5-mm thick) was poured over the sample surface and left to cure. Once the Silastic layer was cured, the walls were removed and the two parts were separated carefully. The Silastic layer was then placed on the working plate, rough surface upwards, and edged again by the same walls. A clear casting resin was poured on top of the Silastic layer and allowed to solidify completely. Once the casting resin was set, the walls were removed and the casting resin was separated carefully from the Silastic layer and polished. As resins are not perfectly rigid materials, being subject to deformation at room temperature, it was not possible to check how accurately the casts represent the original fracture surfaces. Moreover, Vosges sandstone tends to crumble and fracture surfaces lose grains easily; as such, it was not possible to perform a surface topography scan on the original surfaces. To obtain the best representation, several transparent resins were tested, and we chose that having the minimal volumetric-drying effect. We focused our efforts on obtaining reliable local aperture values once the casts were assembled. As will be seen below, the aperture values obtained by image processing are in very good agreement with the volumetric check of the total fracture fluid volumes.

The Vosges sandstone fracture cast was provided with four pressure ports in its centre line. These pressure ports were used for measurements that are not relevant to this study, but they are taken into account in the image processing of the dispersion experiments. Also, screws in the cast holder are accounted for on the Vosges sandstone fracture. The design of granite fracture cast was improved for the dispersion experiments. Thus, only one pressure port was drilled along the centre line of the lower plate and the experimental cell design was enhanced in a way that the screws were placed out of the replica.

The entrance section of the fractures was connected to a distributor (parallelepipedal reservoir) in which the solution and water could be dispersed separately through four ports. These ports are located opposite each other: 4 underneath, 4 on top. The distributor width is equal to the fractures width and its height is 6.5 mm.

The tracer was a methylene blue dye (ACROS ORGANICS Methylene Blue hydrate, pract., 75%), which was found to be a clear and bright tracer in visualization experiments. Placed in a water flow, it offers a good contrast for visualization. The molecular diffusion coefficient of methylene blue in water is $3.1 \pm 0.1 \times 10^{-12} \text{ m}^2/\text{s}$ (Didierjean et al. 1997).

The water and solution density and dynamic viscosity were measured at room temperature (23 °C) using a pycnometer ($\rho_w = 997.1 \text{ kg/m}^3$ and $\rho_s = 997.3 \text{ kg/m}^3$) and a capillary tube ($\mu_w = 0.959 \text{ mPa s}$ and $\mu_s = 0.96 \text{ mPa s}$). The results confirm that addition of the coloring agent did not significantly affect the hydraulic properties of the experimental fluids.

To conduct tracer experiments at room temperature, each fracture was first fully saturated by injecting water at a high flow rate ($1 \times 10^5 \text{ ml/h}$) using a volumetric pump (PCM, EcoMoineau M Series). The distributor was then filled with the solution while avoiding the fracture. Here, the fracture outlet was closed and the solution was injected very slowly into the distributor using the four ports placed underneath. As the distributor filled with the solution, water exited the distributor through the four ports placed on top. Once the distributor was filled with the solution, the fracture outlet was opened and the pumping of the solution at the injected concentration $C_0 = 0.05 \text{ g/l}$ was started at a constant flow rate ($Q = 230 \text{ ml/h}$ for the Vosges sandstone fracture and $Q = 600 \text{ ml/h}$ for the granite fracture) using a low flow rates volumetric pump (Masterflex 7518-00). To achieve a proper initial step injection of the tracer across the fracture inlet, the distributor dimensions (height = 6.5 mm, length = 35 mm, width = fracture width) and the injection flow rates through four ports were chosen to obtain very low fluid velocities within the distributor and thus a homogeneous absolute pressure along the fracture inlet.

Table 1 Fracture characteristics

Fracture	Gravimetric method		Image processing		
	$\langle h \rangle$ (mm)	V_p (ml)	$\langle h \rangle$ (mm)	σ (mm)	V_p (ml)
Vosges sandstone	0.857	33	0.847	0.277	32.6
Granite	0.907	47	0.900	0.283	46.7

During the experiment, the fluids (water and the solution) were drained freely through the exit face of the fracture, which was also connected to a distributor. Afterwards, the fluids were collected into a basin and channeled through a single port, as shown in Fig. 1. The injection was continued until the concentration in the fractures was equal to C_0 .

The injection flow rates were set high enough to make molecular diffusion negligible as compared to tracer advection (6.97 pore volume (V_p) per hour for the Vosges sandstone fracture and 12.77 pore volume per hour for the granite fracture). The corresponding Peclet numbers ($Pe = UL_x/D_m$) were 1.37×10^5 for the Vosges sandstone fracture experiment and 3.46×10^5 for the granite fracture experiment. The value of U is simply $Q/(L_y \langle h \rangle)$, with L_y the fracture width, L_x the fracture length and $\langle h \rangle$ the mean aperture obtained by a gravimetric method in which the fractured are positioned vertically and the mass of water injected in the void space of the fractures is measured. The values of the mean aperture and the average fluid velocity discussed above are presented respectively in Tables 1 and 2.

In both experiments, a series of images were taken at known time intervals for further analysis. Visualization was performed with a CCD camera (Charge coupled Device), resulting in data of 1600×2825 and 1265×2630 pixels after cropping over the fracture area for the Vosges sandstone and granite fractures, respectively. The light source was a Planistar light table, which gives homogeneous and constant lighting. A color filter was used to produce the monochromatic source needed for image processing.

Using these images, the concentration at a given point (x, y) can be determined by image processing based on the attenuation law of Beer–Lambert (Detwiler et al. 1999; Isakov et al. 2001). In this law, the intensity of light passing through a solution varies exponentially with the tracer concentration and the solution thickness. For a given (x, y) position within the fractures, this law can be written as:

$$I(x, y) = I_0(x, y) \exp(-\varepsilon C(x, y)h(x, y)) \tag{9}$$

where I and I_0 are, respectively, light intensities at concentration C , and at zero concentration, ε is the tracer absorptivity, and h is the fracture aperture (solution thickness). Equation 9 can be used to calculate ε , $h(x, y)$, and finally $C(x, y)$ by three-specific experiments, as explained in the next section.

4 Experimental Results

Using a rectangular glass cell with a constant h of 3 mm, ε was first calculated by measuring the intensities at different concentrations. Figure 2 shows measurements done with concentrations varying from 0 to 0.05 g/l and a linear fit using Eq. 9 rewritten in the following form:

$$\ln \left(\frac{I_0}{I} \right) = \varepsilon Ch \tag{10}$$

thus leading to $\varepsilon = 7.867 \pm 0.123 \text{ m}^2/\text{g}$.

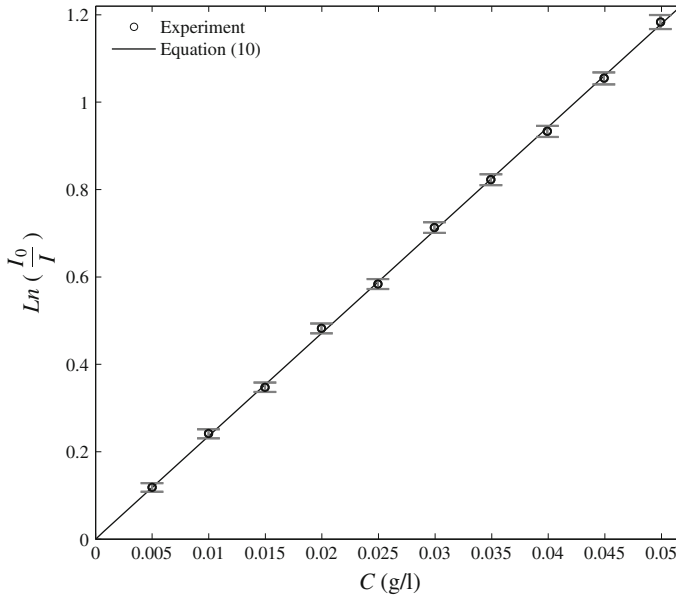


Fig. 2 Tracer absorptivity calibration

The local fracture aperture $h(x, y)$ was then calculated over the entire fracture by taking two images of the fractures, one at zero concentration leading to $I_0(x, y)$ and one at a known concentration ($C_0 = 0.05$ g/l) leading to $I(x, y)$. Knowing $I(x, y)$, $I_0(x, y)$, ε , and $C(x, y) = C_0$, Eq. 9 allows us to calculate $h(x, y)$.

Figure 3 shows the aperture maps of the Vosges sandstone and the granite fractures. The influence of random errors due to the light intensity was reduced by averaging 50 images of each field and using the solution concentration (0.05 g/l) that resulted in minimum total error [see Detwiler et al. (1999) for a detailed review]. The averaged root-mean-square (RMS) aperture measurement errors over the entire fracture field are estimated at 1 and 0.8 % of the mean aperture for the Vosges sandstone and granite fractures, respectively.

The mean value and the standard deviation of the geometric aperture and the total fluid volume of the fractures are summarized in Table 1. These values are in very good agreement with the results of the gravimetric method (within 1.2 % for the Vosges sandstone fracture and within 0.6 % for the granite fracture).

The aperture maps clearly show high spatial variability of the fracture aperture fields. For both fractures, smaller apertures are located at the centre and the larger apertures are located near the inlet and the outlet of the fractures. The lower half of the Vosges sandstone fracture aperture field shows higher variability than the upper half, while for the granite fracture, the spatial variability appears to be relatively high across the entire fracture area.

The aperture data for the Vosges sandstone and granite fractures are displayed as histograms in Fig. 4a, b. The histogram of the Vosges sandstone fracture shows a sharper peak than that for the granite, and the skewness is more positive than for the granite fracture, indicating that more elevations fall below the mean value for this fracture. Also, the kurtosis for the Vosges sandstone fracture indicates a more peaked distribution than that of the granite fracture.

Simply knowing the aperture distributions and their statistics is not sufficient to compare the entire pattern of the fractures void geometry. To investigate the spatial correlation of

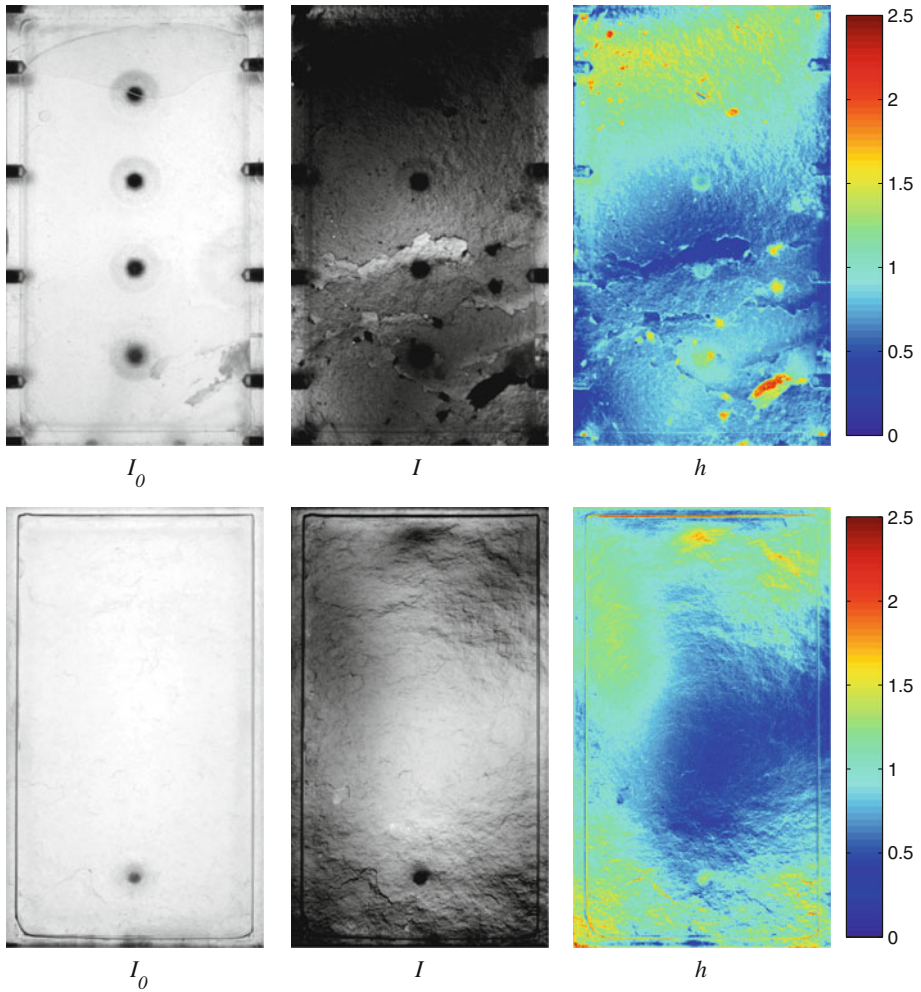


Fig. 3 Aperture map determination: *upper row* Vosges sandstone; *lower row* granite. In image I_0 , the fracture is saturated with water, in image I the fracture is saturated with the solution at C_0 , h is the aperture map in mm

the fractures aperture and finally compare the level of spatial variability of the aperture field, (semi)variogram (γ) analyses were carried out using the Bayesian Maximum Entropy Library/BMELib package (Christakos et al. 2002). A variogram shows the variation between pairs of data as function of the separation (or lag) distance between them. The semi-variogram is calculated as:

$$\gamma(\vec{r}) = \frac{1}{2N_r} \sum_{i=1}^{N_r} (h(\vec{r} + \Delta\vec{r}) - h(\vec{r}))^2 \tag{11}$$

where N_r is the number of pairs.

The omnidirectional experimental semivariograms for the Vosges sandstone and granite fractures are presented in Fig. 4c. The maximum separation distance is approximately one-third the diagonal extent of the fractures. For both fractures, the results show a relatively

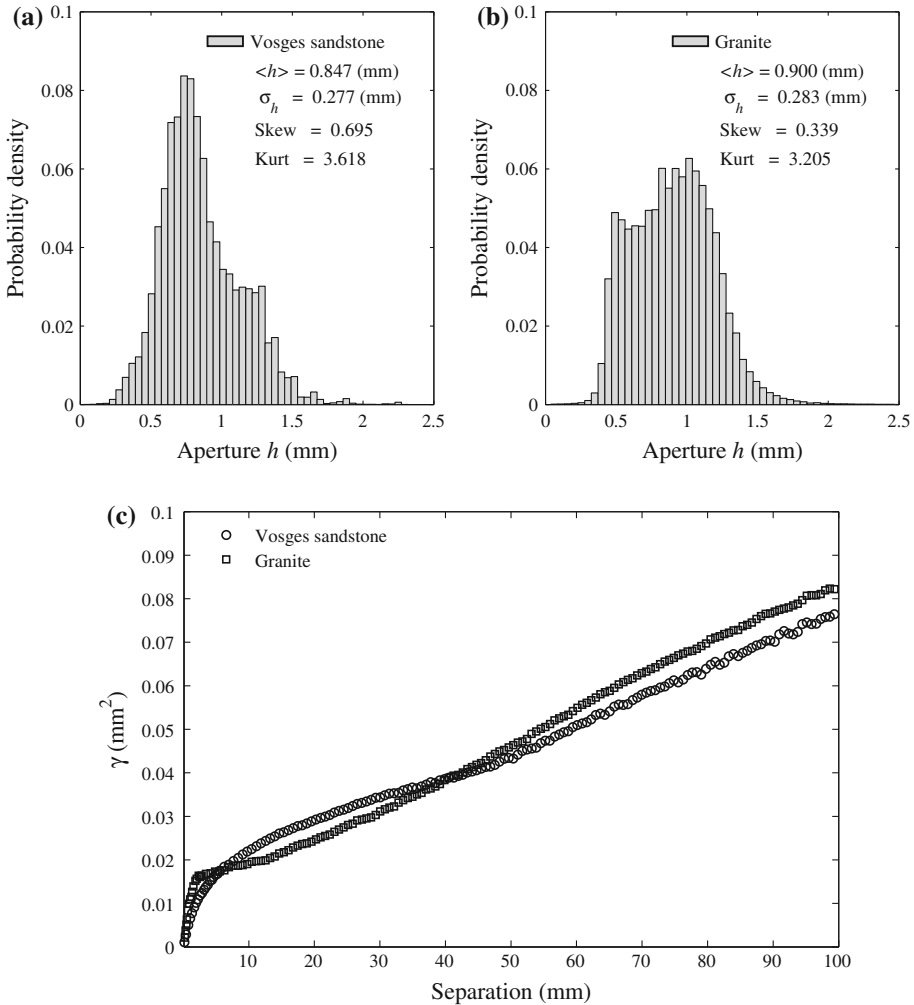


Fig. 4 Histogram and semivariogram of the fracture aperture fields. **a** Histogram of the Vosges sandstone fracture. **b** Histogram of the granite fracture. **c** Experimental semivariograms (omnidirectional) of the fracture aperture fields

strong trend with the separation distances. This can be explained by a high spatial variability of the fracture aperture fields (Fig. 3). The semivariograms indicate that for separation distances between 6 and 40 mm, the semivariogram values are higher for the Vosges sandstone fracture, while outside this range these values are higher for the granite fracture. These higher semivariogram values at distances comparable to the size of the fractures confirm once more that the granite fracture aperture field is more variable (heterogeneous) than the Vosges sandstone one.

Using Eq. 9 and the previous results [i.e., ε and $h(x, y)$], the local 2D instantaneous concentration $C(x, y, t)$ during the tracer injection experiments was calculated. For each fracture, Fig. 5 shows 2D dimensionless concentration maps at six different dimensionless times. The following dimensionless variables were used: dimensionless time $t^* = Qt/V_p$ where V_p is the fracture total fluid volume, dimensionless position $x^* = x/L_x$, and dimen-

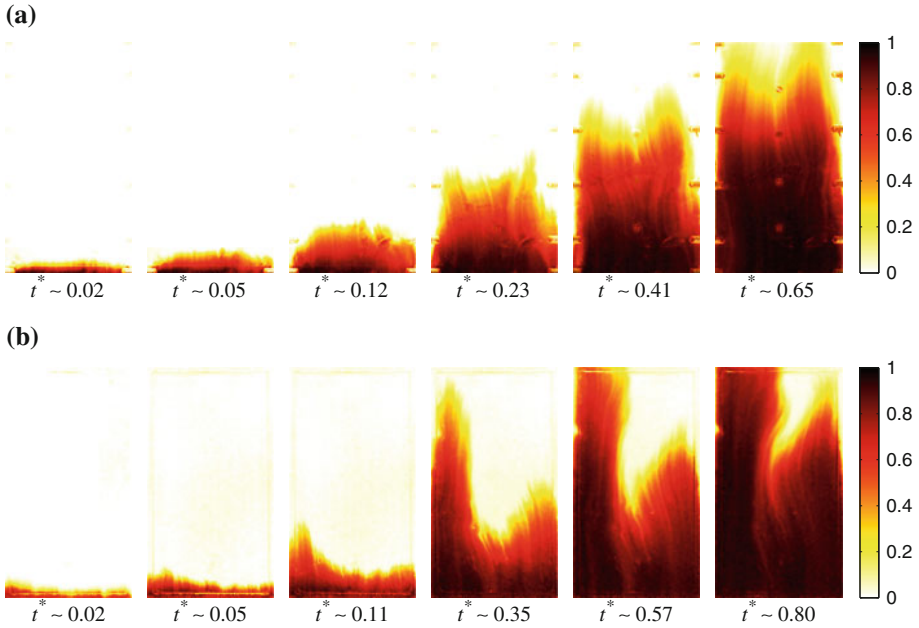


Fig. 5 **a** Tracer experiment for the Vosges sandstone fracture: 2D dimensionless concentration maps at different $t^* = Qt/V_p$ with $Q = 230$ ml/h and $V_p = 33$ ml. Injection is from below. **b** Tracer experiment for the granite fracture: 2D dimensionless concentration maps at different $t^* = Qt/V_p$ with $Q = 600$ ml/h and $V_p = 47$ ml. Injection is from below

sionless concentration $C^* = C/C_0$. As shown in Fig. 5, the concentration fields contain some dark areas, which correspond to the pressure ports, the screws and the cast holders mentioned previously in Sect. 3. All of these artifacts represent less than 1.2% of the Vosges sandstone fracture volume and less than 0.6% of the granite fracture volume.

The effect of the spatial variability of the fracture aperture field on the transport process, especially the constricted areas at the centre of the fractures (dark blue areas in Fig. 3, $h < 0.5$ mm for the Vosges sandstone fracture and $h < 0.75$ mm for the granite fracture), clearly appear in the images of Fig. 5. For the Vosges sandstone fracture (Fig. 5a), the tracer first moves forward homogeneously near the inlet of the fracture ($t^* < 0.12$). After reaching the constricted zone, the solution advances in two preferential flow paths that can be recognized in the fourth ($t^* \sim 0.23$) and fifth ($t^* \sim 0.41$) images. These flow paths grow slowly in the transverse direction but reach the outlet of the fracture almost uniformly ($t^* \sim 0.65$). For the granite fracture, Fig. 5b shows a less uniform tracer front. The third ($t^* \sim 0.11$), fourth ($t^* \sim 0.35$), and fifth ($t^* \sim 0.57$) images show tracer transport in two distinct preferential flow paths, with two different velocity profiles. These flow paths grow more significantly in the transverse direction than those of the Vosges sandstone fracture, and reach the outlet of the fracture with different arrival times ($t^* \sim 0.8$). These results are in agreement with the observation of larger apertures on the left side of the fracture; the first arrival appeared on the left side.

To apply the transport models to the experimental results, 1D dimensionless concentration profiles along the fracture were computed from the 2D concentration fields. The 1D dimensionless concentration profile is defined as the flux-weighted concentration at a given position x (or x^*) from the fracture inlet:

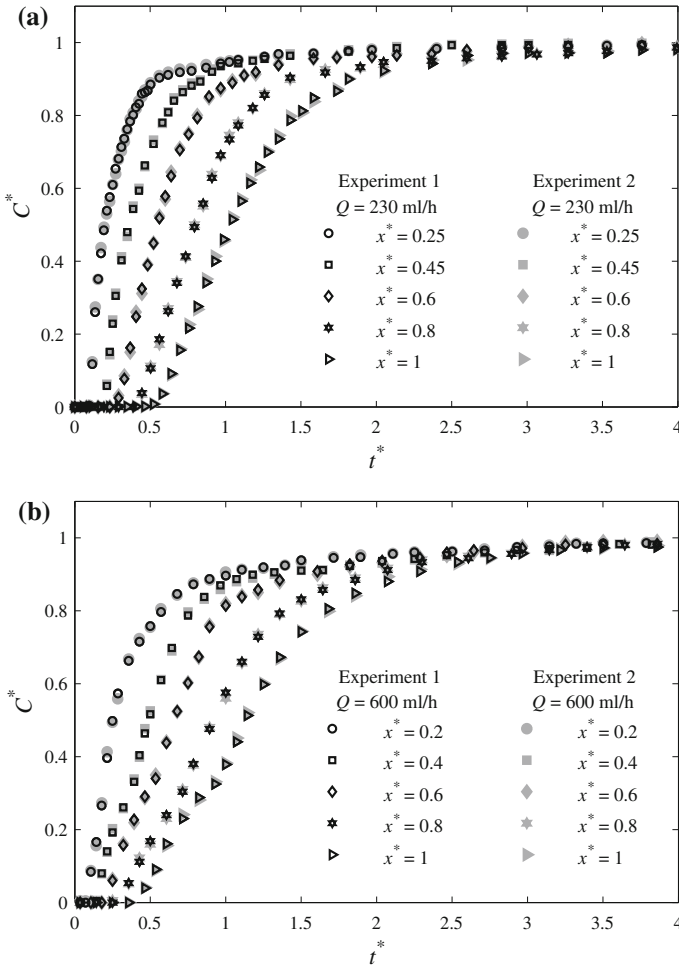


Fig. 6 Concentration profiles versus dimensionless time: **a** Vosges sandstone, **b** granite

$$C^*(x, t) = \frac{\sum_y C(x, y, t) Q(x, y)}{C_0 \sum_y Q(x, y)} \tag{12}$$

where $Q(x,y)$ is the local flow rate obtained using a pore network model (Zimmerman and Bodvarsson 1996):

$$\nabla \cdot (Q) = \nabla \cdot \left(\frac{h^3 \Delta y}{12\mu} \nabla P \right) = 0 \tag{13}$$

where $P(x, y)$ is the local pressure, $h(x, y)$ is the local aperture parallel to the z axis and Δy is the width of a pixel. Equation (13) is commonly known as the local cubic law for fluid flow in a rough-walled fracture.

Figure 6 shows the averaged concentration profiles at five positions ($x^* = 0.2$ (or 0.25), $x^* = 0.4$ (or 0.45), $x^* = 0.6$, $x^* = 0.8$, and $x^* = 1$) as a function of the dimensionless time

for the Vosges sandstone and granite fractures, and for two different experiments carried out under the same experimental conditions. The superimposition of the concentration profiles validates the robustness of the experimental procedure in terms of reproducibility.

The early arrival times and late tails in the concentration profiles are evidence of spatial variability of the fracture aperture field. Comparing the concentration profiles of the fractures, we find earlier arrival times and longer time tailing behaviors for the granite fracture. A less uniform tracer front and thereby both fast and slow preferential flow paths were observed in Fig. 5, for the granite fracture. The tracer reaches the outlet of this fracture shortly after injection ($t^* \sim 0.4$) while this occurs at a larger dimensionless time for the Vosges sandstone ($t^* \sim 0.55$). Moreover, the plume center of mass ($C^* = 0.5$) and the complete saturation of the fractures ($C^* = 1$) occur respectively at dimensionless times $t^* \sim 1.2$ and $t^* \sim 5.5$ for the granite fracture and at dimensionless times $t^* \sim 1$ and $t^* \sim 5$ for the Vosges sandstone fracture. These observations support the finding of smaller arrival times and longer time tailing behaviors in the concentration profiles of the granite fracture, as evident from Fig. 6.

The concentration measurements are affected to random errors due to CCD image noise and solute absorptivity ε and apertures h measurements accuracy. The errors of ε and h are known, however, the transport experiments were instantaneous and thus the concentration measurement errors could not be obtained by averaging multiple images. To estimate these errors, the fractures were sequentially filled with 10 known concentrations varying from 0 to $C_0 = 0.05$ g/l and the root-mean-square errors at each pixel and the averaged errors at each positions x were calculated, respectively. These resulting averaged error profiles were then fitted by least-squares spline to accurately interpolate the averaged RMS error of the concentrations of the transport experiments. The averaged root-mean-square (RMS) error at individual positions ranged from $0.003C_0$ for the 0 g/l in both fractures to $0.011C_0$ and $0.009C_0$ for 0.05 g/l in the Vosges sandstone and the granite fractures, respectively. These values were used to plot the error bars on the BTCs presented in the next section (i.e., Figs. 7 and 8).

5 Modeling Analysis

5.1 Breakthrough Curves at Fracture Outlets

As noted in Sect. 1, experiments are usually performed on non-transparent samples by measuring only the volume production and the outlet breakthrough curves. In this context, fracture transport properties are usually only characterized on a global (domain) scale. In this subsection, for each presented model we study the ability to fit the tracer outlet concentration profiles (i.e., breakthrough curves) and the goodness-of-fits of the estimated parameters. We then use these models in Sects. 5.2 and 5.3 to examine concentration profiles at different dimensionless positions x^* along the fractures.

Figure 7 shows the analytical solutions (Eqs. 4, 5, and 7) fitted to the outlet concentration profiles by allowing all parameters to change in the fitting process. For reference, we show here also solutions using the one-dimensional ADE:

$$\frac{\partial C}{\partial t} = D \frac{\partial^2 C}{\partial x^2} - U \frac{\partial C}{\partial x} \quad (14)$$

where D is the longitudinal hydrodynamic dispersion coefficient related to the dispersivity α and the molecular diffusion of the solute in the fluid D_m by $D = \alpha U + D_m$ (Taylor 1953;

Table 2 Model parameters at position $x^* = 1$ ($Q = 230$ ml/h for the Vosges sandstone fracture and $Q = 600$ ml/h for the granite fracture)

	Vosges sandstone	Granite	Vosges sandstone $Q = 230$ ml/h $U = Q/(L_y(h))$	Granite $Q = 600$ ml/h $U = Q/(L_y(h))$
ADE				
U (m/s)	4.25e-4	8.81e-4	5.03e-4	11.80e-4
D (m ² /s)	8.92e-6	4.25e-5	6.68e-6	4.57e-5
<i>RMSE</i>	1.62	1.90	11.99	11.40
Stratified (normal distribution)				
U (m/s)	4.73e-4	10.49e-4	5.03e-4	11.80e-4
H	0.463	0.427	0.397	0.467
<i>RMSE</i>	1.40	4.29	3.61	6.91
Stratified (lognormal distribution)				
U (m/s)	5.00e-4	11.52e-4	5.03e-4	11.80e-4
H	0.390	0.557	0.385	0.586
<i>RMSE</i>	1.66	1.81	1.88	2.16
CTRW				
u_ψ (m/s)	7.41e-4	22.66e-4		
D_ψ (m ² /s)	3.22e-6	5.83e-5		
β	1.66	1.35		
t_1 (s)	10 ^{0.87}	10 ^{-0.22}		
t_2 (s)	10 ⁴	10 ^{3.2}		
<i>RMSE</i>	0.78	1.79		

Aris 1956). For the case of a continuous injection of a constant concentration, the analytical solution of the ADE is given by Ogata and Banks (1961).

The experimental averaged concentration profiles for the fractures are very close to each other in a complete dimensionless form (C^* vs t^*). Therefore, to better distinguish among the different models, the results are presented as function of time t in Figs. 7, 8, and 9. Moreover, to compare the results of different models in the early breakthrough times and long-time tails, the results are presented in both linear (C^* vs t) and logarithmic ($\log(1 - C^*)$ vs $\log(t)$) scale. The parameter values and the goodness of results are summarized in Table 2. To compare the models, the root-mean-square error (*RMSE*) is used as a criterion to reflect the goodness of fit. It is calculated by:

$$RMSE = 100 \sqrt{\frac{1}{N} \sum_{i=1}^N (C_{ie}^* - C_{im}^*)^2} \tag{15}$$

where C_{ie}^* is the estimated concentration, C_{im}^* is the measured concentration, and N is the number of measured values at a particular observation point.

The results show generally good agreements between the experimental and model concentration profiles (Fig. 7; Table 2). However, the comparison between the measured average velocities and those estimated by the models reveals that the ADE and stratified approach using the normal permeability distribution are unable to estimate correctly the average veloc-

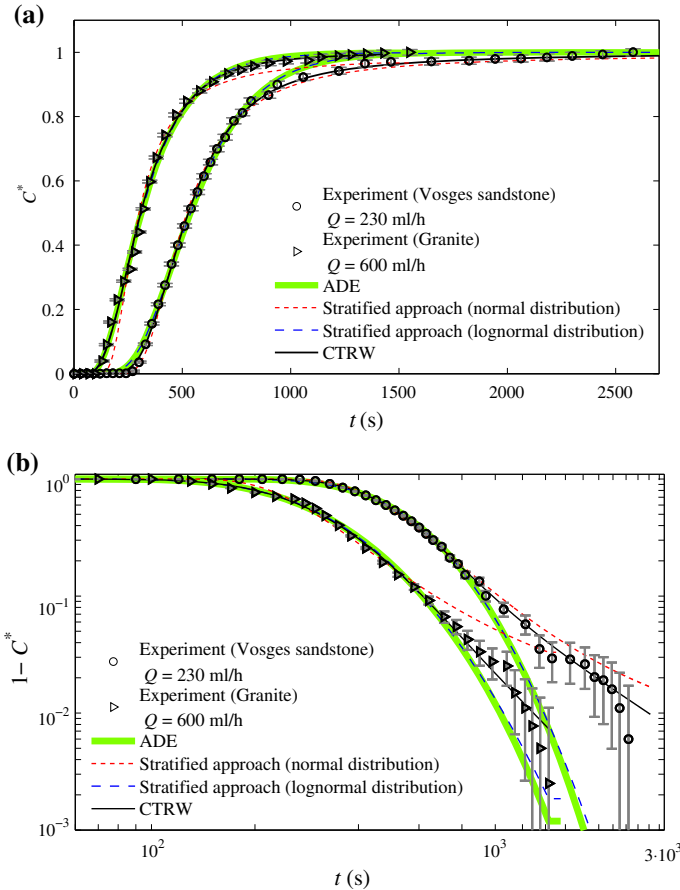


Fig. 7 Outlet average concentration profiles versus time ($Q = 230$ ml/h for the Vosges sandstone fracture and $Q = 600$ ml/h for the granite fracture). Analytical solutions (Eqs. 4, 5, 7, and 14) fitted to the outlet concentration profiles (all parameters change in the fitting process): **a** Linear scale, **b** logarithmic scale. See Table 2 for detailed values

ities; the estimated values are larger than the measured ones for both experiments. To correct this discrepancy, these models were subsequently fitted to the experimental data using the measured average velocity as a given parameter and leaving the dispersion coefficient D and the heterogeneity factor H as the fitting parameters (Fig. 8). Parameter values and goodness of fit in terms of $RMSE$ associated with these results are also summarized in Table 2.

This second fit leads to a significant shift to the right for the advection–dispersion approach, with a very poor match to the data (Fig. 8). As often demonstrated in the literature, the advection–dispersion approach is unable to describe the early arrival time and the long-time tailing behavior characteristic of non-Fickian transport.

For the stratified approach with a normal permeability distribution, this second fit also has a negative effect as the resulting BTC moves away from the experimental BTC for both fractures and for values of C^* in the range of 0–0.9 (i.e., $1 - C^*$ higher than 10^{-1}).

Finally, excepting the long-time tailing region of the experimental BTCs, the stratified approach with a lognormal permeability distribution shows a better agreement with the experimental data in Fig. 8. The model BTCs associated with this approach are almost unaffected

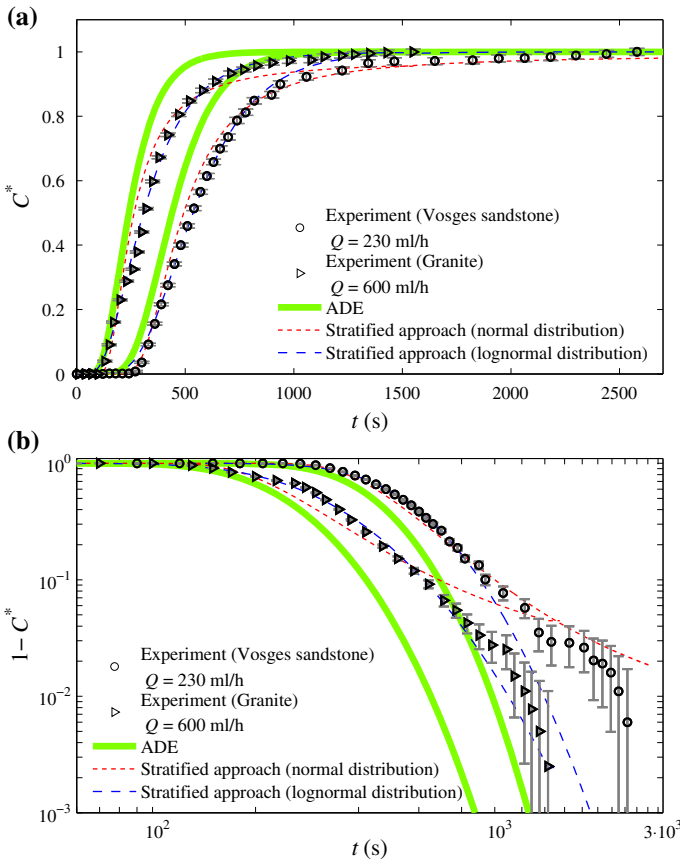


Fig. 8 Outlet average concentration profiles versus time ($Q = 230$ ml/h for the Vosges sandstone fracture and $Q = 600$ ml/h for the granite fracture). Analytical solutions (Eqs. 4, 5, 14) fitted to the outlet concentration profiles using the measured average velocity as a constant and the dispersion coefficient D and the heterogeneity factor H as fitting parameters: **a** Linear scale, **b** logarithmic scale. See Table 2 for detailed values

by the second fit, as confirmed by the *RMSE* values in Table 2. Therefore, the stratification factor values obtained by this approach can be used to quantitatively compare the degree of heterogeneity of the fractures. The higher value of the stratification factor H for the granite fracture suggests that the aperture field of this fracture is more variable than that of the Vosges sandstone fracture. This result is in good agreement with the physical characteristics of the two fractures.

As explained later in Sect. 5.2, the distributions of local permeabilities over the entire fractures are better described by a lognormal distribution than by a normal distribution. While local permeability distributions disregard the spatial correlation of the field, this observation seems to suggest that the permeability distribution of the equivalent medium layers is linked to the local permeability distribution. We will see later that when the local permeabilities follow a normal distribution, BTCs are best fitted by the stratified approach with a normal permeability distribution of the layers.

Considering now the CTRW approach, Fig. 7 clearly shows its ability to characterize tracer transport in the two fractures, agreeing with the experimental data for both the early arrival times and the long-time tailing. Accordingly, CTRW model leads to the lowest *RMSE*

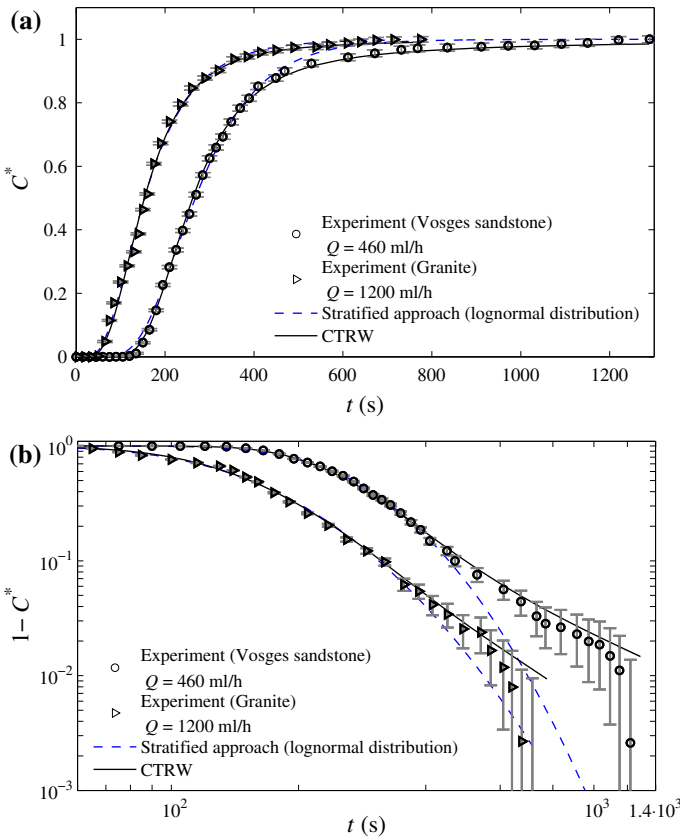


Fig. 9 Outlet average concentration profiles versus time ($Q = 460$ ml/h for the Vosges sandstone fracture and $Q = 1200$ ml/h for the granite fracture). See Table 3 for detailed calculations and values

values in Table 2 for both fractures. The lower value of β for the granite fracture in Table 2 indicates again that this fracture is more heterogeneous than the Vosges sandstone fracture. For our experiments, we obtain transport velocities higher than the mean fluid velocities. As explained above, the transport velocity may be larger or smaller than the average fluid velocity. The difference between these two velocities arises because of the way that the velocities are averaged; in contrast to the definition of average fluid velocity U , the average transport velocity u_{ψ} is defined as the first moment of the transition length probability distribution function, $p(s)$, divided by a characteristic time. The presence of preferential paths can explain an average transport velocity higher than the average fluid velocity. Tracer injected in the vicinity of a preferential path will allow much of the tracer to travel through the fracture at higher velocity; this tracer is excluded from the other regions where water is present, yielding a higher average tracer velocity relative to that of the fluid (Kuntz et al. 2011).

Table 2 summarizes the parameter values and the goodness of the results presented in this subsection, and confirms that the equivalent-stratified medium and the CTRW approaches characterize non-Fickian transport features in the two fractures.

To demonstrate the robustness of the estimated parameters of these approaches, a second set of experiments was carried out at different flow rates and the estimated parameters (see Table 2) were used to model the resulting averaged concentration profiles. Figure 9 shows

the concentration profiles at the outlet of the fractures. Details of the parameters and their values calculated from the analytical solutions (Eqs. 5, 7) are summarized in Table 3. The *RMSE* values confirm that the estimated values (Table 2) can be used to model the averaged concentration profiles at different flow rates.

To this point, the equivalent stratified medium and the CTRW approaches were tested at the outlet of the fractures. As noted above, in the next sections we study individually the suitability of these approaches to fit the concentration profiles at different positions along the length of the fractures.

5.2 The equivalent-stratified medium approach

As explained in Sect. 2.1, the fundamental equation of the stratified approach (Eq. 1) assumes that the permeability of layers of the equivalent stratified medium is randomly distributed and follows a given probability distribution function (normal or lognormal distribution law). The permeability of each layer is constant at medium scale but can change from one layer to another. Here, the transport can be characterized by a constant heterogeneity factor H , and the average tracer front velocity can be given by the measured average fluid velocity. Figure 10a, b shows the stratified normal and lognormal distribution approaches (Eqs. 4, 5) fitted to the outlet concentration profile and plotted at four distances with the heterogeneity factor calculated at $x^* = 1$ for the Vosges sandstone and granite fractures, respectively. The associated root-mean-square error (*RMSE*) values are listed in Table 4.

Experimental and model concentration profiles in Fig. 10a and their corresponding *RMSE* values in Table 4 show that the stratified normal and lognormal distribution approaches better fit the measured concentration profiles, respectively, at distances $x^* = 0.25, 0.45$ and 0.6 and at distances $x^* = 0.8$ and 1 for the Vosges sandstone fracture. Except for some discrepancies during the intermediate and late times at $x^* = 0.25$ and the late times at $x^* = 0.8$, the agreement between the experimental results at each distance and its associated (normal or lognormal) approach is generally satisfactory. However, a reliable criterion to choose the suitable permeability distribution at a given location in the fractures is needed.

The differences between the results using the normal and lognormal distributions might be related to the difference in the distribution of local permeabilities from the inlet to a given position in the fracture. Figure 11 shows the distributions of local permeabilities ($k(x, y) = h^2(x, y)/12$) over the inlet and four distances ($x^* = 0.25, 0.5, 0.75$ and 1) for the Vosges sandstone fracture. The distributions are also fitted by normal and lognormal distributions and the determination coefficient r^2 (shown in Fig. 11) is used as a criterion to reflect the goodness of fits. The distribution of local permeabilities follows the normal law in the first half of this fracture, as shown in Fig. 11a, b. Then, for $x^* > 0.5$, the distributions change progressively their forms and become completely lognormal for $x^* > 0.7$, as shown in Fig. 11c, d.

From these results, one can conclude that the applicability of the stratified normal and lognormal approaches at a given position in a fracture depends on the distribution of the local permeabilities between the inlet and that position. This finding is corroborated by the results on the granite fracture experiment. Figure 10b and the corresponding *RMSE* values in Table 4 indicate that the stratified lognormal distribution approach yields better fits than those of the stratified normal distribution approach, at all distances x^* for this fracture. Also, in agreement with these results, the distribution of local permeabilities follows the lognormal law along the entire fracture, as shown in Fig. 12.

Although the stratified lognormal distribution better captures the concentration profiles for this fracture, the goodness of fit is not satisfactory as x^* decreases, especially below 0.6 .

Table 3 The equivalent-stratified medium approach (lognormal distribution) and the CTRW parameter values at position $x^* = 1$ ($Q = 460$ ml/h for the Vosges sandstone fracture and $Q = 1200$ ml/h for the granite fracture)

	Vosges sandstone			Granite		
	$Q_1 = 230$ ml/h	$Q_2 = 2 \times Q_1 = 460$ ml/h		$Q_1 = 600$ ml/h	$Q_2 = 2 \times Q_1 = 1200$ ml/h	
	Stratified (lognormal distribution)					
U (m/s)	$U_1 = 5.03e - 4$	$U_2 = 2 \times U_1 = 10.06e - 4$		$U_1 = 11.80e - 4$	$U_2 = 2 \times U_1 = 23.60e - 4$	
H	$H_1 = 0.385$	$H_2 = H_1 = 0.385$		$H_1 = 0.586$	$H_2 = H_1 = 0.586$	
$RMSE$	1.88	1.89		2.16	2.05	
CTRW						
u_{ψ} (m/s)	$u_{\psi 1} = 7.41e - 4$	$u_{\psi 2} = 2 \times u_{\psi 1} = 14.82e - 4$		$u_{\psi 1} = 22.66e - 4$	$u_{\psi 2} = 2 \times u_{\psi 1} = 45.32e - 4$	
D_{ψ} (m ² /s)	$D_{\psi 1} = 3.22e-6$	$D_{\psi 2} = 2 \times D_{\psi 1} = 6.44e - 5$		$D_{\psi 1} = 5.83e - 5$	$D_{\psi 2} = 2 \times D_{\psi 1} = 11.66e - 5$	
β	$\beta_1 = 1.66$	$\beta_2 = \beta_1 = 1.66$		$\beta_1 = 1.35$	$\beta_2 = \beta_1 = 1.35$	
t_1 (s)	$t_{11} = 10^{0.87}$	$t_{12} = 0.5 \times t_{11} = 10^{0.57}$		$t_{11} = 10^{-0.22}$	$t_{12} = 0.5 \times t_{11} = 10^{-0.52}$	
t_2 (s)	$t_{21} = 10^4$	$t_{22} = t_{21} = 10^4$		$t_{21} = 10^{3.2}$	$t_{22} = t_{21} = 10^{3.2}$	
$RMSE$	0.78	0.93		1.79	1.86	

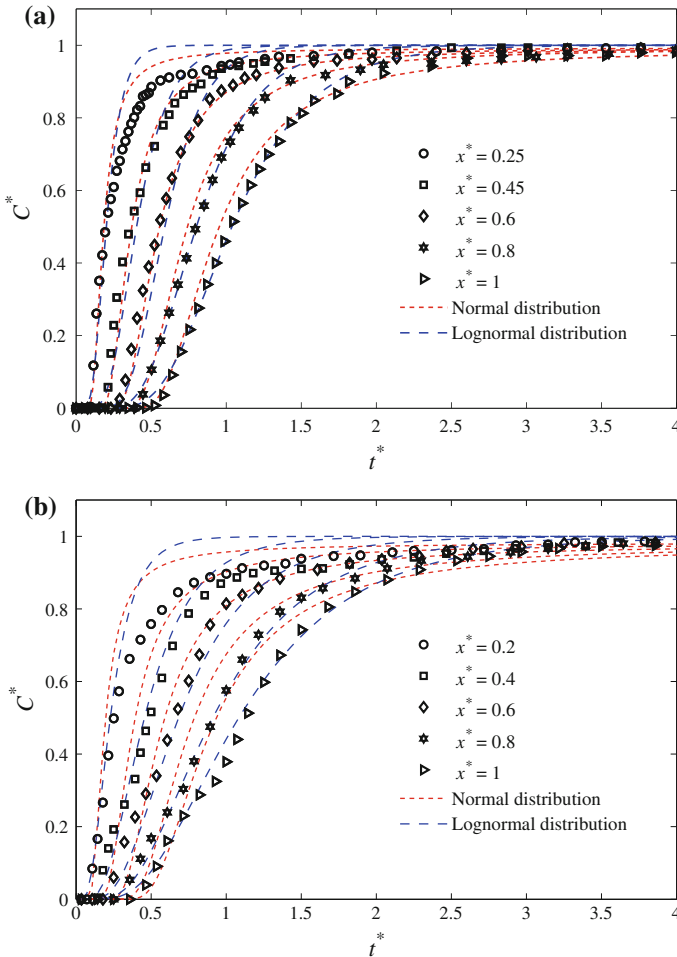


Fig. 10 Stratified model fitted to the concentration profiles at different positions using the measured average velocity and the heterogeneity factor H calculated at $x^* = 1$: **a** Vosges sandstone; **b** granite

As discussed in Sect. 4, this might be due to the high level of spatial variability of the aperture field of this fracture which cannot be accurately modeled using a single parameter model (i.e., the heterogeneity factor H). A simple way to increase the ability of the stratified approach to model tracer transport in the fractures is to consider any fracture portion between the inlet and a given position as a heterogeneous medium itself, leading to a position-dependent heterogeneity factor (see Fourar and Radilla 2009).

Figure 13a, b shows the stratified normal and lognormal distribution approaches (Eqs. 4, 5) fitted to the concentration profiles at different distances respectively for the Vosges sandstone and granite fractures using the measured average velocity as constant and leaving the heterogeneity factor H as the single fitting parameter. As expected, the individually fitted curves better describe the experimental concentration profiles. Values of H and $RMSE$ are listed in Table 4. The performance of individual fits is indicated by the smaller $RMSE$ values of individual fits than the predicted ones with the heterogeneity factor H calculated at $x^* = 1$. Here again, the applicability of the stratified normal and lognormal approaches at each position

Table 4 The equivalent-stratified medium approach stratification factor H and CTRW β values and goodness-of-fit at five x^* distances

Voges sandstone											
Position	Stratified (Normal distribution)			Stratified (Lognormal distribution)			CTRW				
	$H = H(x^* = 1)$	$H = 0.397(x^*)^{-0.148}$	RMSE	$H = H(x^* = 1)$	$H = 0.385(x^*)^{-0.480}$	RMSE	$\beta = \beta(x^* = 1)$	RMSE	$\beta = \beta(x^*)$	RMSE	
1	3.61	0.397	3.61	1.88	0.385	1.88	0.78	1.66	0.78	0.78	
0.8	3.14	0.403	3.04	2.53	0.428	2.38	1.09	1.67	1.08	1.08	
0.6	2.43	0.410	2.31	5.35	0.500	4.97	1.28	1.67	1.25	1.25	
0.45	3.62	0.430	2.73	5.22	0.575	4.74	2.17	1.68	2.01	2.01	
0.25	7.91	0.495	3.83	9.68	0.731	4.93	4.84	1.61	2.85	2.85	
Granite											
Position	Stratified (Normal distribution)			Stratified (Lognormal distribution)			CTRW				
	$H = H(x^* = 1)$	$H = 0.467(x^*)^{-0.163}$	RMSE	$H = H(x^* = 1)$	$H = 0.586(x^*)^{-0.285}$	RMSE	$\beta = \beta(x^* = 1)$	RMSE	$\beta = \beta(x^*)$	RMSE	
1	6.91	0.467	6.91	2.16	0.586	2.16	1.79	1.35	1.79	1.79	
0.8	5.13	0.485	5.11	1.81	0.601	1.77	1.55	1.36	1.51	1.51	
0.6	4.31	0.497	4.25	3.76	0.621	3.47	2.93	1.38	2.23	2.23	
0.4	6.62	0.543	5.87	4.29	0.775	2.83	3.97	1.32	3.14	3.14	
0.2	9.01	0.599	7.43	8.53	0.910	4.37	8.14	1.27	4.94	4.94	

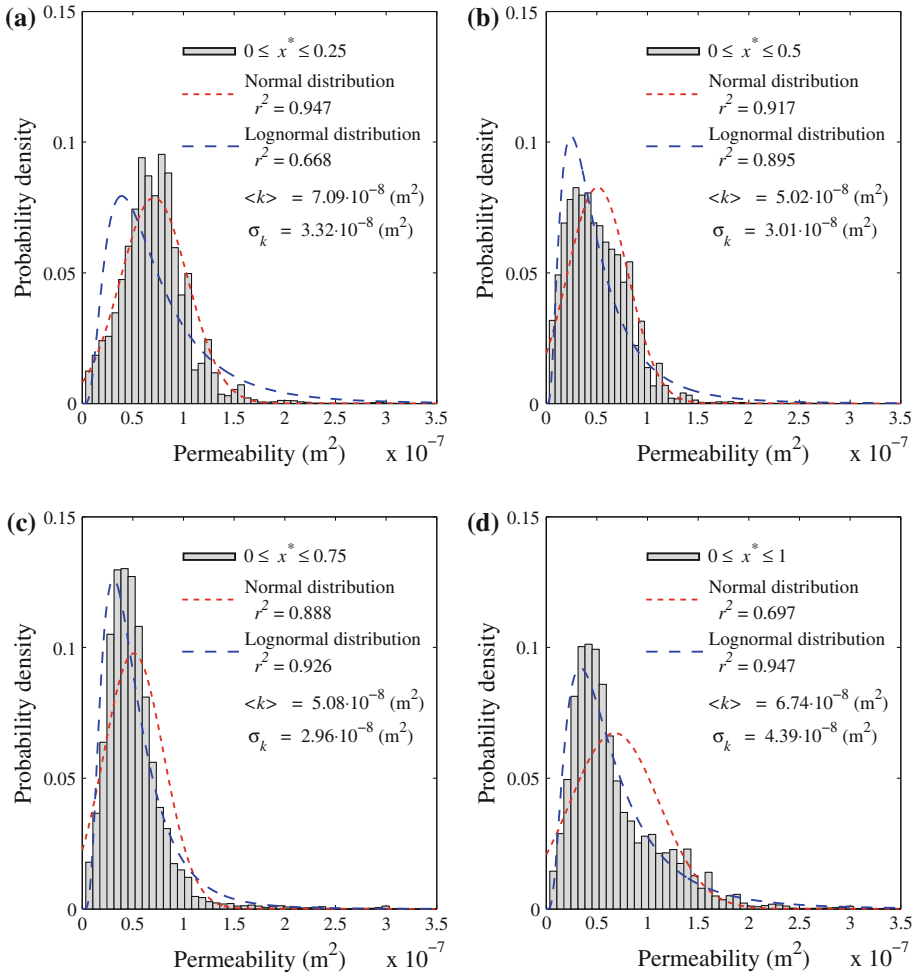


Fig. 11 The distribution of local permeabilities between the inlet and the positions $x^* = 0.25$, $x^* = 0.5$, $x^* = 0.75$, and $x^* = 1$ for the Vosges sandstone fracture. The distributions are fitted by normal and lognormal distributions

is in agreement with the distribution of the local permeabilities between the inlet and this position.

Figure 14 shows the evolution of experimental values of H as a function of the dimensionless length of the fractures. It appears that the heterogeneity factor H is a decreasing function of the distance from the fracture inlets. The fractures at the inlet can be considered as stratified and therefore, H has its maximum value. As the tracer advances through the fractures, the flow becomes three-dimensional and the stratification effect of the fractures decreases. The stratification factor tends to a constant value near the outlet of both fractures. Figure 14 shows the stratification factor to be a power law of the dimensionless distance from the fracture inlet:

$$H = a(x^*)^b \tag{16}$$

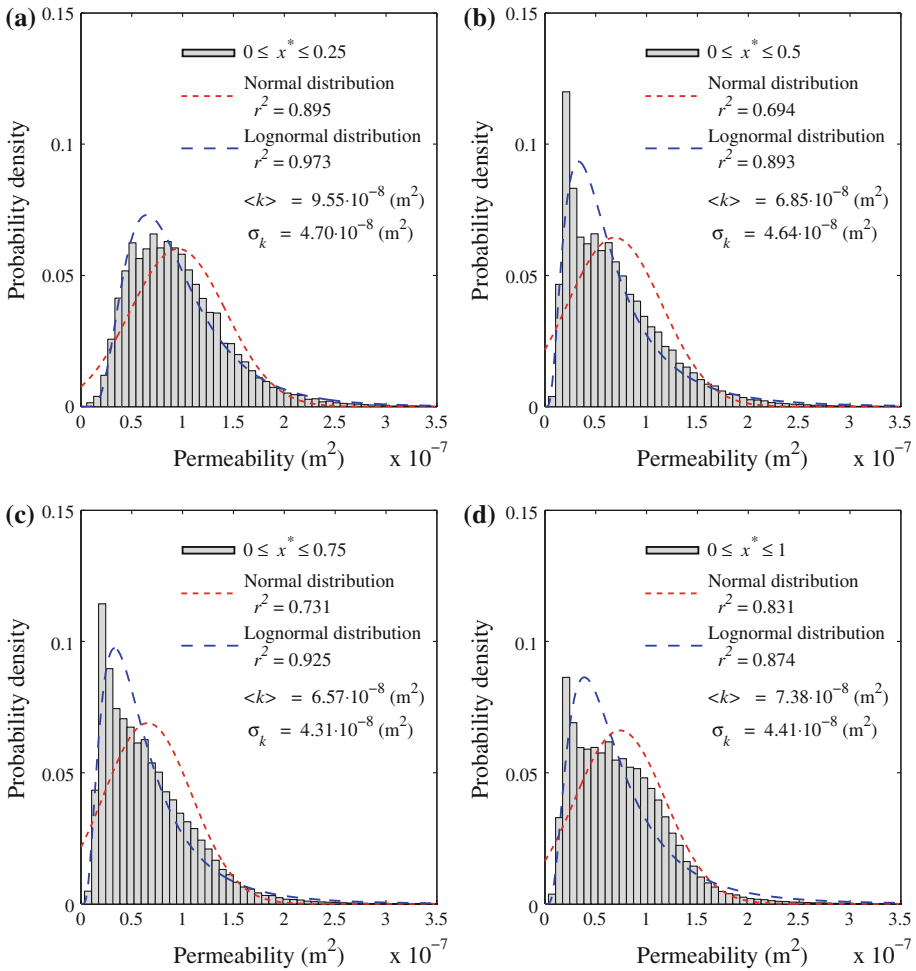


Fig. 12 The distribution of local permeabilities between the inlet and the positions $x^* = 0.25$, $x^* = 0.5$, $x^* = 0.75$, and $x^* = 1$ for the granite fracture. The distributions are fitted by normal and lognormal distributions

The associated values of parameters a and b are presented in Table 4. By comparing the values for a , the stratification factor values at $x^* = 1$, the fractures can be classified according to their degree of heterogeneity. These results are consistent with the study of Fourar and Radilla (2009) on heterogeneous porous media.

The stratified approach leads to fairly good results: its main advantage is that it provides a good estimate of the average fluid velocity and also gives insight into the distribution of local permeabilities of a given heterogeneous medium. Moreover, the stratification factor H can be used to quantify the degree of heterogeneity of the fracture. However, this approach is unable to describe correctly the long-time tailing behaviors associated with non-Fickian transport (the stratified normal and lognormal distribution approaches underestimate and overestimate the concentration values, respectively). This is mainly due to the inherent assumption of the present work which considers two simple and commonly used permeability distributions defined by a single parameter (i.e., normal and lognormal distributions). Searching for a

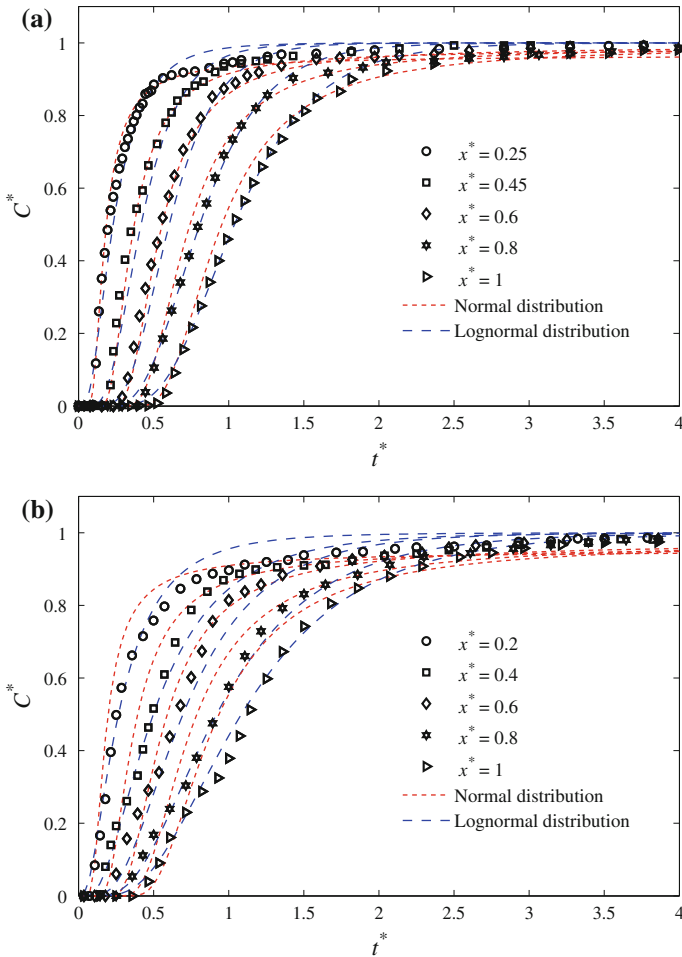


Fig. 13 Stratified model fitted to the concentration profiles at different positions leaving the heterogeneity factor H as a single fitting parameter: **a** Vosges sandstone; **b** granite

more complex permeability distribution of layers for which the resulting BTCs better fit the experimental BTCs is certainly possible, but beyond the scope of the present work.

5.3 The CTRW approach

Using the CTRW approach, it is possible to match breakthrough curves measured at different positions with a single set of u_ψ , D_ψ , β , t_1 , and t_2 ; obtained from a fit to the outlet concentration profile. Our results confirm that for both fractures, $1 < \beta < 2$, so that the average tracer velocity is constant in time; therefore, the CTRW transport equation (Eq. 7) with TPL probability rate is fitted to the outlet concentration profile and plotted at four additional positions, as shown in Fig. 15. The associated $RMSE$ values are listed in Table 4. Compared to the stratified normal and lognormal approaches, the CTRW approach provides better results with a single set of parameters. The performance of the CTRW approach is also reflected by smaller $RMSE$ values, as evident from Table 4.

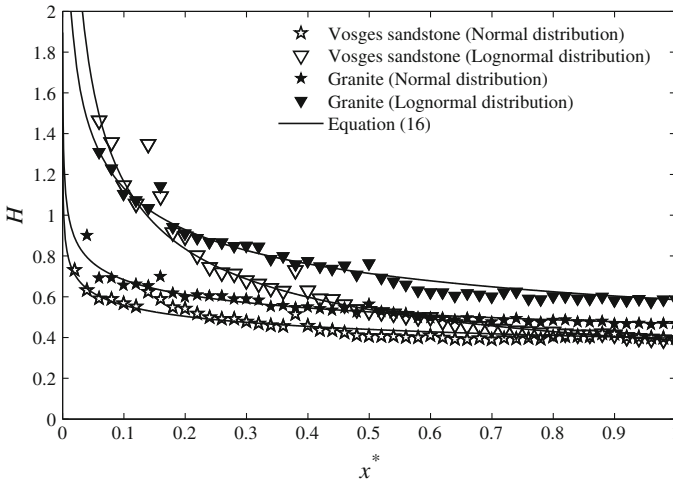


Fig. 14 Heterogeneity factor H versus the dimensionless distance x^*

Figure 15a and the associated *RMSE* values in Table 4 indicate that the predictions of the CTRW approach are generally in very good agreement with the experimental concentration profiles of the Vosges sandstone fracture, except some discrepancies during the early and intermediate times at $x^* = 0.25$. It is important to note that all three modeling approaches considered here are averaged approaches, so that in all cases, the tracer must experience sufficient heterogeneities (i.e., x^* must be sufficiently large) to allow a meaningful application by “average concentration” estimates from the model. Therefore, it is somewhat normal that the CTRW approach, and also the stratified normal and lognormal distributions approaches, cannot describe correctly the concentration profile near the outlet of the fractures only by the parameters obtained from the outlet concentration profile. This feature can also be confirmed by the experimental and predicting results of the granite fracture. As shown in Fig. 15b and Table 4, the goodness of fits increases significantly as x^* decreases, especially below 0.6.

As explained in Sect. 2.2, the TPL transition time distribution function is a key aspect of the CTRW approach, which characterizes the nature of the transport by the value of β . The nature of the transport in a fracture depends obviously on the configuration of the heterogeneities. Therefore, an individual value of β at each x^* can be used to explain the effect of the spatial variability of the fracture aperture fields on the nature of the transport between the inlet and different distances.

Figure 16a, b shows the CTRW approach (Eq. 7) fitted to the concentration profiles at different distances using the u_ψ , D_ψ , t_1 , and t_2 , calculated from the outlet concentration profile, as constants and leaving β as the single fitting parameter for the Vosges sandstone and granite fractures, respectively. The estimated values of β and the goodness of fit at different distances are listed in Table 4. For both fractures, the results do not change significantly except at $x^* = 0.25$ for the Vosges sandstone fracture and $x^* = 0.2$ for the granite fracture. As can be seen in Table 4, the estimated values of β are very close to the values obtained from the outlet concentration profiles at $x^* > 0.2$. This behavior shows stability in the flow at the fracture scale, which is in agreement with the CTRW framework that assumes stationary statistical properties even though the fracture aperture fields are highly variable. The lower values of β at x^* near the inlet (consistent also with the higher values of the stratification factor H in this region), indicate the strong impact of the local heterogeneities on transport near the fracture inlets.

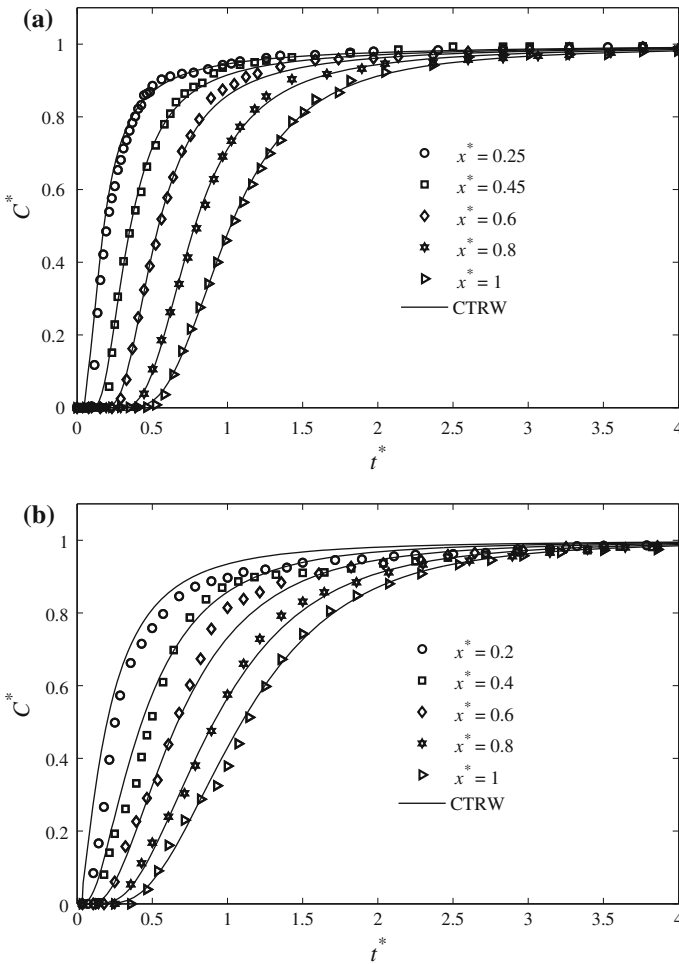


Fig. 15 CTRW model (Eq. 7) fitted to the outlet concentration profiles and plotted at four other positions: **a** Vosges sandstone; **b** granite

The results demonstrate the ability of CTRW to characterize anomalous transport in the fractures. This approach accounts for a broad spectrum of tracer transition rates in heterogeneous media, and as a consequence, it is capable of correctly capturing the early arrival times and the long-time tailing. Moreover, the CTRW parameters D_ψ , β and t_2 can be used to characterize the nature of tracer transport in the fractures and to compare relative degrees of fracture heterogeneity. For our experiments, the higher value of dimensionless dispersion coefficient for the granite fracture shows that the transport is more dispersive: $D_\psi^* = D_\psi / (u_\psi L_x)$ is 0.017 for the Vosges sandstone fracture and 0.078 for the granite fracture. The lower values of β for the granite fracture show again that the aperture map of this fracture is more variable than the Vosges sandstone fracture. For both experiments, the values of cut-off time t_2 are very large compared to the duration of the experiment (2580 s for the Vosges sandstone fracture experiment and 1550 s for the granite fracture experiment), indicating that transition to Fickian transport has not yet occurred.

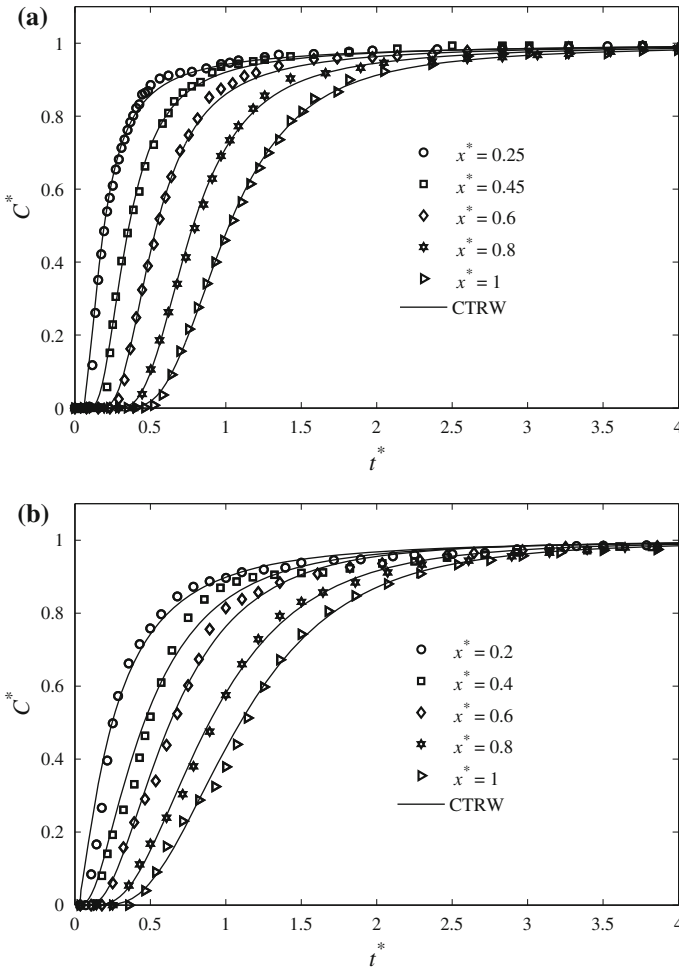


Fig. 16 CTRW model (Eq. 7) fitted to the concentration profiles using the u_ψ , D_ψ , β , t_1 and t_2 of the outlet concentration profile and leaving exponent β as the single fitting parameter: **a** Vosges sandstone; **b** granite

6 Conclusions

Tracer test experiments were conducted through replicas of two real fractures. The experiments were interpreted with three different approaches to evaluate their ability to describe the transport behaviors and to relate model parameters to fracture heterogeneity. In particular, we evaluated the advantages and disadvantages of the stratified and CTRW approaches in terms of their ability to describe the evolution of breakthrough curves determined at several distances from the inlet.

The results indicated that the classical advection–dispersion model is not appropriate for modeling early arrival and long-time tailing, as a result of the inherent heterogeneity of the fractures and the resulting non-Fickian transport behavior. In contrast, the stratified model with one spatially dependent parameter better captured the evolution of anomalous breakthrough curves. Using this approach, the average fluid velocity and the distribution law of

local permeabilities can be determined for a medium. Also, the heterogeneity factor H can be used to examine the degree of heterogeneity. However, the stratified approach associated with a single parameter permeability distribution cannot explain the long-time tailing adequately, and the H factor is space-dependent and determined from detailed information on the permeability distribution. Developing more complex (multi parameter) permeability distributions would certainly lead to better fits of the experimental BTCs and is therefore a potentially promising path to be explored in the future. The CTRW, based on estimated parameters obtained from the outlet breakthrough curve, provided excellent description of the full evolution of the breakthrough curves. The coefficient β appears as a consistent parameter to characterize the heterogeneity. Further study is needed to identify the relationship between the tracer transport velocity and the mean fluid velocity.

References

- Aris, R.: On the dispersion of a solute particle in a fluid moving through a tube. *Proc. R. Soc. London. Ser. A.* **235**, 67–77 (1956)
- Bauget, F., Fourar, M.: Non-Fickian dispersion in a single fracture. *J. Contam. Hydrol.* **100**(3–4), 137–148 (2008). doi:[10.1016/j.jconhyd.2008.06.005](https://doi.org/10.1016/j.jconhyd.2008.06.005)
- Becker, M.W., Shapiro, A.M.: Tracer transport in fractured crystalline rock: evidence of nondiffusive breakthrough tailing. *Water Resour. Res.* **36**(7), 1677–1686 (2000). doi:[10.1029/2000WR900080](https://doi.org/10.1029/2000WR900080)
- Berkowitz, B., Cortis, A., Dentz, M., Scher, H.: Modeling non-Fickian transport in geological formations as a continuous time random walk. *Rev. Geophys.* **44**, RG2003 (2006). doi:[10.1029/2005RG000178](https://doi.org/10.1029/2005RG000178)
- Berkowitz, B., Kosakowski, G., Margolin, G., Scher, H.: Application of continuous time random walk theory to tracer test measurements in fractured and heterogeneous porous media. *Ground Water* **39**(4), 593–604 (2001). doi:[10.1111/j.1745-6584.2001.tb02347.x](https://doi.org/10.1111/j.1745-6584.2001.tb02347.x)
- Berkowitz, B., Scher, H.: Anomalous transport in random fracture networks. *Phys. Rev. Lett.* **79**(20), 4038–4041 (1997). doi:[10.1103/PhysRevLett.79.4038](https://doi.org/10.1103/PhysRevLett.79.4038)
- Berkowitz, B., Scher, H.: Exploring the nature of non-Fickian transport in laboratory experiments. *Adv. Water Res.* **32**(5), 750–755 (2008). doi:[10.1016/j.advwatres.2008.05.004](https://doi.org/10.1016/j.advwatres.2008.05.004)
- Berkowitz, B., Scher, H., Silliman, S.E.: Anomalous transport in laboratory scale, heterogeneous porous media. *Water Resour. Res.* **36**(1), 149–158 (2000). doi:[10.1029/1999WR900295](https://doi.org/10.1029/1999WR900295)
- Bolster, D., Valdés-Parada, F.J., LeBorgne, T., Dentz, M., Carrera, J.: Mixing in confined stratified aquifers. *J. Contam. Hydrol.* **120–120**, 198–212 (2010). doi:[10.1016/j.jconhyd.2010.02.003](https://doi.org/10.1016/j.jconhyd.2010.02.003)
- Brown, S.R., Caprihan, A., Hardy, R.: Experimental observation of fluid flow channels in a single fracture. *J. Geophys. Res.* **103**(B3), 5125–5132 (1998). doi:[10.1029/97JB03542](https://doi.org/10.1029/97JB03542)
- Christakos, G., Bogaert, P., Serre, M.L.: *Temporal GIS: Advanced Functions for Field-Based Applications*. Springer, New York (2002)
- Communar, G.M.: A solute transport in stratified media. *Transp. Porous Media* **31**(2), 133–134 (1998). doi:[10.1023/A:1006557032656](https://doi.org/10.1023/A:1006557032656)
- Dentz, M., Cortis, A., Scher, H., Berkowitz, B.: Time behavior of solute transport in heterogeneous media: transition from anomalous to normal transport. *Adv. Water Resour.* **27**(2), 155–173 (2003). doi:[10.1016/j.advwatres.2003.11.002](https://doi.org/10.1016/j.advwatres.2003.11.002)
- Detwiler, R.L., Pringle, S.E., Glass, R.J.: Measurement of fracture aperture fields using transmitted light: an evaluation of measurement errors and their influence on simulations of flow and transport through a single fracture. *Water Resour. Res.* **35**(9), 2605–2617 (1999). doi:[10.1029/1999WR900164](https://doi.org/10.1029/1999WR900164)
- Detwiler, R., Rajaram, H., Glass, R.J.: Solute transport in variable aperture fractures: An investigation of the relative importance of Taylor dispersion and macrodispersion. *Water Resour. Res.* **36**(7), 1611–1625 (2000). doi:[10.1029/2000WR900036](https://doi.org/10.1029/2000WR900036)
- Didierjean, S., Amaral Souto, H.P., Christian, Moyné C.: Dispersion in periodic porous media. Experience versus theory for two-dimensional systems. *Chem. Eng. Sci.* **52**(12), 1861–1874 (1997). doi:[10.1016/S0009-2509\(96\)00518-0](https://doi.org/10.1016/S0009-2509(96)00518-0)
- Dronfield, D.G., Silliman, S.E.: Velocity dependence of dispersion for transport through a single fracture of variable roughness. *Water Resour. Res.* **29**(10), 3477–3483 (1993). doi:[10.1029/93WR01407](https://doi.org/10.1029/93WR01407)
- Fourar, M.: Characterization of heterogeneities at the core-scale using the equivalent stratified porous medium approach. In: *Proceedings of the International Symposium of the Society of Core Analysts, Trondheim, 12–16 Sept 2006*

- Fourar M., Radilla G. (2009) Non-Fickian description of tracer transport through heterogeneous porous media. *Transp. Porous Media* **(80)**3:561–579. doi:[10.1007/s11242-009-9380-7](https://doi.org/10.1007/s11242-009-9380-7)
- Gao, G., Zhan, H., Feng, S., Huang, G., Mao, X.: Comparison of alternative models for simulating anomalous solute transport in a large heterogeneous soil column. *J. Hydrol.* **377**(3–4), 391–404 (2009). doi:[10.1016/j.jhydrol.2009.08.036](https://doi.org/10.1016/j.jhydrol.2009.08.036)
- Güven, O., Molz, F.J., Melville, J.G.: An analysis of macrodispersion in a stratified aquifer. *Water Resour. Res.* **20**(10), 1337–1354 (1984). doi:[10.1029/WR020i010p01337](https://doi.org/10.1029/WR020i010p01337)
- Hakami, E., Larsson, E.: Aperture measurements and flow experiments on a single natural fracture. *Int. J. Rock Mech. Min. Sci. Geomech. Abstr* **33**(4), 395–404 (1996). doi:[10.1016/0148-9062\(95\)00070-4](https://doi.org/10.1016/0148-9062(95)00070-4)
- Ippolito, I., Hinch, E.J., Daccord, G., Hulin, J.P.: Tracer dispersion in 2-D fractures with flat and rough walls in a radial flow geometry. *Phys. Fluids A* **5**(8), 1952–1962 (1993). doi:[10.1063/1.858822](https://doi.org/10.1063/1.858822)
- Isakov, E., Ogilvie, S.R., Taylor, C.W., Glover, P.W.J.: Fluid flow through rough fractures in rocks I: high resolution aperture determinations. *Earth Planet. Sci. Lett.* **191**(3–4), 267–282 (2001). doi:[10.1016/S0012-821X\(01\)00424-1](https://doi.org/10.1016/S0012-821X(01)00424-1)
- Iwano, M., Einstein, H.H.: Stochastic analysis of surface roughness, aperture and flow in a single fracture. In: *Proceedings of the International Symposium EUROCK '93*, pp. 135–141, Lisbon (1993)
- Jiménez-Hornero, F.J., Giráldez, J.V., Laguna, A., Pachepsky, Y.: Continuous time random walks for analyzing the transport of a passive tracer in a single fissure. *Water Resour. Res.* **41**, W04009 (2005). doi:[10.1029/2004WR003852](https://doi.org/10.1029/2004WR003852)
- Johns, R.A., Steude, J.S., Castanier, L.M., Roberts, P.V.: Nondestructive measurements of fracture aperture in crystalline rock cores using X-ray computed tomography. *J. Geophys. Res.* **98**(B2), 1889–1900 (1993). doi:[10.1029/92JB02298](https://doi.org/10.1029/92JB02298)
- Kosakowski, G., Berkowitz, B., Scher, H.: Analysis of field observations of tracer transport in a fractured till. *J. Contam. Hydrol.* **47**(1), 29–51 (2001). doi:[10.1016/S0169-7722\(00\)00140-6](https://doi.org/10.1016/S0169-7722(00)00140-6)
- Kuntz, B.W., Rubin, S., Berkowitz, B., Singha, K.: Quantifying solute transport at the Shale Hills Critical Zone Observatory. *Vadose Zone J.* **10**(3), 843–857 (2011). doi:[10.2136/vzj2010.0130](https://doi.org/10.2136/vzj2010.0130)
- Levy, M., Berkowitz, B.: Measurement and analysis of non-Fickian dispersion in heterogeneous porous media. *J. Contam. Hydrol.* **64**(3–4), 203–226 (2003). doi:[10.1016/S0169-7722\(02\)00204-8](https://doi.org/10.1016/S0169-7722(02)00204-8)
- Margolin, G., Berkowitz, B.: Application of continuous time random walks to transport in porous media. *J. Phys. Chem.* **B104**(16), 3942–3947 (2000). doi:[10.1021/jp993721x](https://doi.org/10.1021/jp993721x)
- Moreno, L., Neretnieks, I., Eriksen, T.: Analysis of some laboratory tracer runs in natural fissures. *Water Resour. Res.* **21**(7), 951–958 (1985). doi:[10.1029/WR021i007p00951](https://doi.org/10.1029/WR021i007p00951)
- Moreno, L., Tsang, Y.W., Tsang, C.F., Hale, F.V., Neretnieks, I.: Flow and tracer transport in a single fracture: a stochastic model and its relation to some field observations. *Water Resour. Res.* **24**(12), 2033–2048 (1988). doi:[10.1029/WR024i012p02033](https://doi.org/10.1029/WR024i012p02033)
- Neretnieks, I., Eriksen, T., Tahtinen, P.: Tracer movement in a single fissure in granitic rock: some experimental results and their interpretation. *Water Resour. Res.* **18**(4), 849–858 (1982). doi:[10.1029/WR018i004p00849](https://doi.org/10.1029/WR018i004p00849)
- Nordqvist, A.W., Tsang, Y.W., Tsang, C.F., Dverstorp, B., Andersson, J.: Effects of high variance of fracture transmissivity on transport and sorption at different scales in a discrete model for fractured rocks. *J. Contam. Hydrol.* **22**(1–2), 39–66 (1996). doi:[10.1016/0169-7722\(95\)00064-X](https://doi.org/10.1016/0169-7722(95)00064-X)
- Ogata, A., Banks, R.B.: A solution of the differential equation of longitudinal dispersion in porous media. *U.S. Geol. Survey, Professional Papers*, 411-A, pp. A1–A7 (1961)
- Oron, A.P., Berkowitz, B.: Flow in rock fractures: The local cubic law assumption re-examined. *Water Resour. Res.* **34**(11), 2811–2825 (1998). doi:[10.1029/98WR02285](https://doi.org/10.1029/98WR02285)
- Pyrak-Nolte, L.J., Montemagno, C.D., Nolte, D.D.: Volumetric imaging of aperture distributions in connected fracture networks. *Geophys. Res. Lett.* **24**(18), 2343–2346 (1997). doi:[10.1029/97GL02057](https://doi.org/10.1029/97GL02057)
- Radilla, G., Sausse, J., Sanjuan, B., Fourar, M.: Interpreting tracer tests in the enhanced geothermal system (EGS) of Soultz-sous-Forêts using the equivalent stratified medium approach. *Geothermics* (2012). doi:[10.1016/j.geothermics.2012.07.001](https://doi.org/10.1016/j.geothermics.2012.07.001)
- Sharifzadeh, M., Mitani, Y., Esaki, T., Urakawa, F.: An investigation of joint aperture distribution using precise surface asperities measurement and GIS data processing. In: Ohnishi Y., Aoki K. (eds.) *Proceedings of the 3rd International Asian Rock Mechanics Symposium*, pp. 165–171, Kyoto (2004)
- Taylor, G.I.: Dispersion of soluble matter in solvent flowing slowly through a tube. *Proc. R. Soc. London. Ser. A.* **219**, 186–203 (1953)
- Tsang, C.F., Tsang, Y.W., Hale, F.V.: Tracer transport in fractures: analysis of field data based on a variable-aperture channel model. *Water Resour. Res.* **27**(12), 3095–310 (1991). doi:[10.1029/91WR02270](https://doi.org/10.1029/91WR02270)
- Wan, J., Tokunaga, T.K., Orr, T.R., O'Neill, J., Connors, R.W.: Glass casts of rock fracture surfaces: a new tool for studying flow and transport. *Water Resour. Res.* **36**(1), 355–360 (2000). doi:[10.1029/1999WR900289](https://doi.org/10.1029/1999WR900289)

- Xiong, Y., Huang, G., Huang, Q.: Modeling solute transport in one-dimensional homogeneous and heterogeneous soil columns with continuous time random walk. *J. Contam. Hydrol.* **86**(3–4), 163–175 (2006). doi:[10.1016/j.jconhyd.2006.03.001](https://doi.org/10.1016/j.jconhyd.2006.03.001)
- Yeo, I.W.: Effect of fracture roughness on solute transport. *Geosciences J.* **5**(2), 145–151 (2001). doi:[10.1007/BF02910419](https://doi.org/10.1007/BF02910419)
- Zavala-Sanchez, V., Dentz, M., Sanchez-Vila, X.: Characterization of mixing and spreading in a bounded stratified medium. *Adv. Water Resour.* **32**(5), 635–648 (2009). doi:[10.1016/j.advwatres.2008.05.003](https://doi.org/10.1016/j.advwatres.2008.05.003)
- Zimmerman, R.W., Bodvarsson, G.S.: Hydraulic conductivity of rock fractures. *Transp. Porous Media* **23**(1), 1–30 (1996). doi:[10.1007/BF00145263](https://doi.org/10.1007/BF00145263)